Multi-technique physico-chemical characterization of particles generated by a gasoline engine: Towards measuring tailpipe emissions below 23 nm

Cristian Focsa, Dumitru Duca, J.A. Noble, M. Vojkovic, Y. Carpentier, C. Pirim, C. Betrancourt, Pascale Desgroux, T. Tritscher, J. Spielvogel, et al.

Multi-technique physico-chemical characterization of particles generated by a gasoline engine: towards measuring tailpipe emissions below 23 nm

C. Focsa[a,*], D. Duca[a], J. A. Noble[a,1], M. Vojkovic[a], Y. Carpentier[a], C. Pirim[a], C. Betrancourt[b,2], P. Desgroux[b], T. Tritscher[c], J. Spielvogel[c], M. Rahman[d], A. Boies[d], K. F. Lee[e], A. N. Bhave[e], S. Legendre[f], O. Lancry[f], P. Kreutziger[g], M. Rieker[g]

[a] *University of Lille, CNRS, UMR 8523 – PhLAM – Laboratoire de Physique des Lasers Atomes et Molécules, F-59000 Lille, France*
[b] *University of Lille, CNRS, UMR 8522 – PC2A – Laboratoire de Physico-Chimie des Processus de Combustion et de l'Atmosphère, F-59000 Lille, France*
[c] *TSI GmbH, 52068 Aachen, Germany*
[d] *University of Cambridge, CB2 1PZ Cambridge, United Kingdom*
[e] *CMCL Innovations, Castle Park, CB3 0AX Cambridge, United Kingdom*
[f] *HORIBA Scientific, 59650 Villeneuve d'Ascq, France*
[g] *HORIBA Europe GmbH, Landwehrstrasse 55, D-64293, Darmstadt, Germany*

Abstract

Particulate emissions from on-road motor vehicles are the focus of intensive current research due to the impact of the ambient particulate matter (PM) levels on climate and human health. Constant improvement in engine technology has led to significant decrease in the number and mass of emitted PM, but particular concern is raised nowadays by the ultrafine particles. In this context, there is a critical lack of certification procedures for the measurement of the smallest-size (<23 nm) particulate matter emissions. To support the engine development process as well as future certification procedures, a measurement technology for sub-23 nm particles must be designed. The development of a reliable measurement procedure entails understanding the formation and evolution of particles from the engine to the tailpipe via multiple analytical techniques and theoretical simulations.

We present here extensive experimental characterization of ultrafine particles emitted by a gasoline direct injection single-cylinder engine as particle generator. The particles were sampled using a cascade impactor which allows size-separation into 13 different size bins. Chemical characterization of the collected size-selected particles was performed using mass spectrometry, which gives access to detailed molecular information on chemical classes of critical interest such as organosulphates, oxygenated hydrocarbons, nitrogenated hydrocarbons, metals, or polycyclic aromatic hydrocarbons. Additionally, the morphology of the emitted particles was probed with atomic force (AFM) and scanning electron microscopy (SEM). Tip-Enhanced Raman Spectroscopy (TERS) was applied for the first time to sub-10nm combustion-generated particles to gather information on their nanostructure. The extensive database built from these multiple experimental characterizations has been used as input of a theoretical approach to simulate and validate engine out-emissions. These studies were performed in the framework of the H2020 PEMS4Nano project which aims to the development of a robust, reliable and reproducible measurement technology for particles down to 10 nm for both chassis dyno and real driving emissions (RDE).

Keywords: Internal combustion engine, nanoparticles, physico-chemical characterization, mass spectrometry, emission modeling

*Corresponding author: cristian.focsa@univ-lille.fr
[1] Present address: CNRS, Aix Marseille Université, PIIM, UMR 7345, 13397 Marseille cedex, France
[2] Present address: Ecole Centrale Supélec, 91190 Gif-sur-Yvette, France

1. Introduction

The particulate matter (PM) is a ubiquitous air pollutant, consisting of a mixture of solid and liquid particles that can remain suspended in the air, ranging from a few minutes up to days or even weeks depending on their size, and hence undergo long-range transport (World Health Organization, 2013). Primary PM can have anthropogenic sources which include PM produced by internal combustion (IC) engines (*e.g.* on-road vehicles), wear of vehicle components, or industrial activities. Traffic is therefore a significant source of PM emission having a mass size distribution ranging from coarse mode ($PM_{10} < 10\ \mu m$) to fine mode ($PM_{2.5} < 2.5\ \mu m$) particles (Atkinson et al., 2010), and often dominated by submicron particles (*e.g.* $PM_{0.5} < 0.5\ \mu m$). Major improvements in engine technology and the use of alternative fuels over the last few years have helped contain the environmental harm caused by PM emissions (Raza et al., 2018). While NO_x and hydrocarbons emissions have been reduced along with the mass and number of emitted particles, one of the downsides has been the shift in the particle diameter towards smaller sizes (lower than 100 nm (Karjalainen et al., 2014)), thus likely contributing to air pollution, *i.e.* a public health issue (*e.g.* Manke et al. (2013); Sager and Castranova (2009); Seaton et al. (2009); EPA (2009)). The G-20 countries account for 90% of global vehicle sales, and 17 out of the 20 members have chosen to follow the European regulatory pathway for vehicle emissions control (Williams and Minjares, 2016). Therefore, information about the particle number (PN) of ultrafine particles is becoming more and more valuable for vehicle certification. Specifically, sub-23 nm particles have recently attracted a lot of attention for mainly two reasons. For one, sub-23 nm particles can be produced, and sometimes in high concentrations, in both diesel and gasoline direct injection (GDI) engines (*e.g.* Giechaskiel et al. (2014)). Second, the harmfulness of the particles has been shown to correlate better with surface area than with mass (Donaldson et al., 1998; Oberdorster, 1996), which becomes important for ultrafine particles even though their residence time in the atmosphere is shorter. However, it has been estimated that the percentage of sub-23 nm solid particles that is not measured by current certification procedures (that have a cut-off size of 23 nm) could reach 30-40% of the total PN for gasoline vehicles utilizing direct injection, and be potentially higher when alternative fuels are being used (Giechaskiel et al., 2017). Therefore, the critical lack of certification procedures for the measurement of ultrafine (< 23 nm) particulate matter emissions should be addressed. Current efforts (Kontses et al., 2020; Chasapidis et al., 2019; Lee et al., 2019) focus on providing solid scientific ground to allow lowering the 23 nm limit to 10 nm, with the aims of providing robust particle number measurement methodology and associated instrumentation. Although possible in principle (at least in well-controlled laboratory conditions), going below this limit appears as very challenging as nanometer-size particles raise important sampling, measurement and quantification issues which can result in undesired biases and artifacts (Simonen et al., 2019). This difficulty is of course enhanced when designing reliable portable measurement systems dedicated to monitoring nanoparticle emissions in real-driving conditions.

The development of a robust and reliable certification procedure for measuring even small particles requires a good understanding of the characteristics of the emitted particles. There are several studies that examine particle emissions of modern direct injection engines during laboratory tests (chassis dynomometer) and even under real driving conditions. The number, mass, and size distribution of emitted particles have been already studied for a wide variety of engine operating conditions (Khalek et al., 2010; Baral et al., 2011; Maricq et al., 2011; Karjalainen et al., 2014; Vojtíšek et al., 2014; Momenimovahed et al., 2015; Ko et al., 2019). It was also shown that engine emissions tend to be optimized for the certification test cycle, while other regimes are often overlooked (Vojtisek-Lom et al., 2009; Weiss et al., 2011). As a result, engine emissions in real driving conditions (RDE) tend to be higher (Kayes et al., 2000; Kristensson et al., 2004). The chemical composition of exhaust particles was also examined and enabled the estimation of fuel and oil contribution to elemental (EC) and organic carbon (OC) (Kleeman et al., 2008; Fushimi et al., 2016; An et al., 2016). However, there is still very little information about the chemical composition of fine and ultrafine particles emitted by modern engines and their origin. The latter is especially important for the development of a Particle Measurement Program (PMP) capable of measuring ultrafine particles, below 23 nm (Zheng et al., 2011).

To explore the physico-chemical characteristics of the emitted particles, it is necessary to perform a multi-technique analysis of GDI engine emissions. The objective of this study is to build a large database through a

thorough size-dependent physico-chemical characterization of a wide variety of combustion-generated particles sampled under different engine operating conditions. The database includes extensive information about the size-dependent molecular-level chemical composition of emitted particles as small as 10 nm obtained with high-performance mass spectrometry techniques. Recently developed advanced statistical methodologies (Irimiea et al., 2018, 2019; Duca et al., 2019), based on principal component analysis (PCA) and hierarchical clustering analysis (HCA), are used in this work to highlight subtle differences, as well as similarities, between different-sized particles. These data are complemented by the particle morphology information obtained with a scanning electron microscope (SEM) and an atomic force microscope (AFM), while unprecedented tip-enhanced Raman spectroscopy (TERS) measurements on individual combustion-generated particles down to a few nm are performed to gather insights about their nanostructure. Engine set-points used for off-line characterization of particles were selected using laser induced incandescence (LII) – an on-line measurement technique able to provide real-time information on the PM size-distribution and volume fraction. The obtained database is then utilized in a theoretical approach (referred to as Model Guided Application – MGA) which combines detailed physico-chemical simulation together with advanced statistical techniques of parameter estimation, computational surrogate generation and sensitivity analysis (Lee et al., 2019). The MGA aims to predict the particle formation in the engine, as well as particle dynamics in the exhaust system and sampling line. Although the modeling work presented in this paper is related to a single-cylinder test engine (used as a particle generator), the knowledge gained here (experimental and theoretical) can be easily transferred to multi-cylinder engines and even expanded to drive cycle simulations, thus providing crucial information for the development and optimization of particle emission monitoring systems (PEMS). These studies were carried out in the framework of the H2020 PEMS4Nano project (`www.pems4nano.eu`) where a bottom-up approach was adopted in order to develop a robust, reliable and reproducible particle emission monitoring system (PEMS) for both chassis dyno and real-driving conditions.

2. Materials and Methods

2.1. Single cylinder engine and sampling line

The particulate matter investigated in this work was produced by a generic gasoline direct injection single-cylinder test engine, whose specifications are given in Table 1. The engine was operating on Euro Stage V E5 Gasoline (CEC-RF-02-08 E5). The temperature for both coolant and oil (Agip SIGMA, 10W-40) was set to 80°C. All the operating points studied are described in Table 2 (*e.g.* applied load, injection timing). For all the set-points, the engine was operating at 2000RPM with the ignition timing set for the maximum brake torque (MBT). Between each operating point, the engine was operated with methane (CH_4) for 30 minutes to ensure the cleanliness of the combustion chamber.

Table 1: Engine specifications (b/aTDC – before/after Top Dead Center)

Specification		**Value**
Cylinder head		Pentroof type
Compression ratio		12.5:1
Bore		82 mm
Stroke		85 mm
Stroke volume		449 cm^3
Fuel direct injection system		Central mounted generic six-hole injector
Injection pressure		150 bars
Spark plug location		Exhaust side
Intake valve timing:	Open	334 deg. bTDC
	Close	166 deg. bTDC
Exhaust valve timing:	Open	154 deg. aTDC
	Close	330 deg. aTDC

Monitoring and sampling of particles from the generic single-cylinder test engine was performed using a home-built sampling line. A partial flow was taken from the exhaust duct approximately 5 cm after

the exhaust port and was then supplied via 8 cm long transfer line to DEKATI FPS 4000 (Fine Particle Sampler) two-stage dilution system (1:3 and 1:10 dilution ratios for the hot (180°C) and cold (35°C) dilution stages respectively). The rest of the exhaust flows through an optical cell for on-line soot monitoring by LII. As detailed below, the LII technique was used for preliminary characterization and selection of the engine operating conditions. Additionally, the in-cylinder pressure profile and gas phase emissions (CO, μHC and NO_x) were monitored.

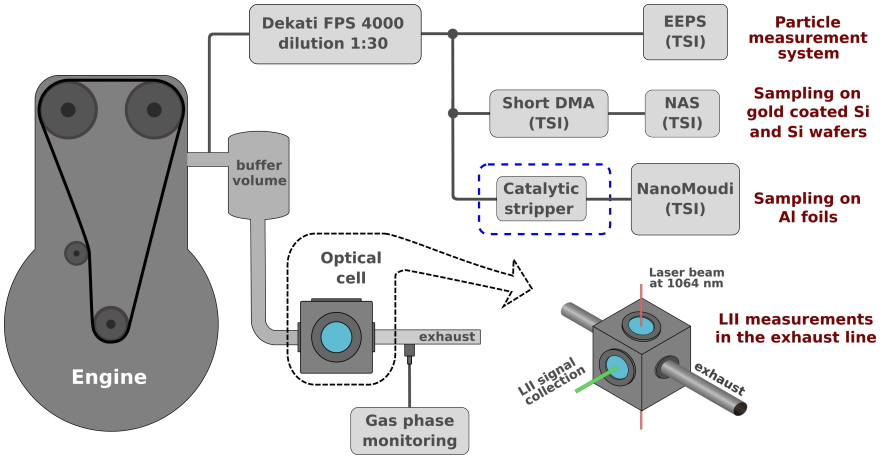

Figure 1: Schematic representation of the sampling line. Sampling with NanoMoudi on Al foils can be done with or without the catalytic stripper (dashed blue rectangle).

After dilution, the flow of particles was split into three branches. On the first one, an Engine Exhaust Particle Sizer (EEPS; TSI, model 3090) was used to measure particle number and size distribution. A combination of a Nano-Differential Mobility Sizer (Nano-DMA; TSI, model 3085) and a Nanometer Aerosol Sampler (NAS; TSI, model 3089, Fig. 1), placed on the second branch, was used to collect particles for structural and morphological analyses, thus enabling sampling within very narrow size bins. Finally, the sampling for chemical analysis was conducted on the third branch with a NanoMOUDI II cascade impactor (TSI/MSP, model 125R). Being a "Micro-Orifice Uniform-Deposit Impactor", the NanoMoudi works on the well-known principle of inertial impaction (Marple et al., 1991; Marple, 2004). The MOUDI impactors have sharp stage characteristics with steep cut-offs and low inter-stage wall losses. The used model comprises 13 stages, with nominal cut-off sizes of 10000, 5600, 3200, 1800, 1000, 560, 320, 180, 100, 56, 32, 18, and 10 nm. Particles were deposited on uncoated aluminum foils (heated for 12 hours in an oven at 300°C prior to the sampling).

A catalytic stripper (CS) can be placed before the NanoMoudi in order to investigate its impact on the properties of the particles sampled in several engine regimes. The CS was built by the University of Cambridge in a similar fashion to the commercially-available models (Catalytic Instruments). The coating was commercially available precious metal loading (100–300 g/m^2) with an alumina wash coat. The CS was calibrated and monitored with a temperature controller to ensure that the centerline temperature of the aerosol achieves 350°C prior to entering the catalytic monolith contained within the device. The catalytic stripper performance in terms of hydrocarbon removal was tested to be >99% for 30 nm tetracontane particles at a concentration of $>10^4$ cm^{-3}. The precise catalyst chemistry has not been measured. The penetration efficiency was >60% for 10 nm particles and the entire system residence time was 1–2 s. The influence of the catalytic stripper on particle characteristics was studied since its usage in a PMP compliant system and is preferred over an evaporative tube (ET) as it significantly reduces the number of artifact ultrafine particles formed by renucleation of semivolatiles, thus considerably increasing the reliability of the system (Zheng et al., 2011). The stripper was operating at 370°C and was preheated prior to the sampling.

The off-line characterization techniques used for structural and morphological analysis (described in section 2.3.1) require samples with a low coverage, *i.e.* isolated individual particles. At the same time, the chemical characterization (Section 3.3) requires more loaded samples, ideally with a homogeneous layer of

particles fully covering the deposition substrate. Consequently, the sampling time for the samples intended for chemical characterization was much longer. Moreover, to obtain similar coverages, the time was optimized for each engine operation regime, the longest (12h) being for the **NHC** regime and the shortest (6h) for the **EM** one, respectively (Table 2). Regarding the samples intended for the structural and morphological analysis, the collection time varies between 30 minutes and 1h, depending on engine conditions.

Table 2: Studied engine operating points (IMEP – Indicated Mean Effective Pressure, λ – ratio of the actual air/fuel ratio to stoichiometric). "Optimal engine conditions" refer to optimal injection and ignition timings set for MBT.

Set-point	**IMEP, bar**	λ **± 0.01**	**Injection deg. BTDC**	**Comments**
NS	3	1.01	270	
NM	6	1.01	270	
NH	12	1.01	270	
NHC	12	1.01	270	With a catalytic stripper
OM	6	1.01	270	Addition of oil
EM	6	0.70	270	Low air/fuel ratio
EI1	12	1.01	305	Early injection
EI2	12	1.01	311	Early injection

"N" in the set-point designations stands for normal engine operation (optimal engine conditions); "S/M/H" – small/medium/high load applied to the engine; "C" – catalytic stripper; "OM", "EM" – malfunction regimes ("O" – addition oil; "E" – excess of fuel resulting in low air/fuel ratio);
"EI" – optimal air/fuel ration, high load, early injection.

2.2. On-line characterization by Laser-Induced Incandescence

LII is a laser-based technique allowing soot concentration monitoring in various environments, for instance in flames (Schulz et al., 2006) and in the combustion chamber of internal combustion engines (Boiarciuc et al., 2007; de Francqueville et al., 2010; Koegl et al., 2018). LII also proved to be suitable to control real time soot emission directly in the exhausts of diesel (Case and Hofeldt, 1996; Bachalo et al., 2002), gasoline (Smallwood et al., 2001; Bardi et al., 2019), and aeronautical engines (Delhay et al., 2009). In this work, the objective of the LII measurements is to study the evolution of the soot volume fraction with engine conditions in order to select the appropriate engine set-points for off-line soot-characterization. The principle of LII consists first in heating combustion-generated particles up to 3500-4200K, generally using a pulsed laser, and then recording the radiation associated with the thermal emission while they cool down. This incandescence emission follows the Planck law and depends on the emission properties of particles at the detection wavelength. LII is mainly used to determine the soot volume fraction (f_ν) and the primary particle diameter (Schulz et al., 2006). Soot volume fraction can be determined from the time-resolved LII peak signal as follows:

$$f_\nu \propto \left(\frac{LII}{E(m_\lambda) \cdot B(T,\lambda)} \right) \tag{1}$$

where $B(T,\lambda)$ is the Planck function, T is the peak reached temperature, λ - the emission wavelength, m_λ - the refractive index of the particle and $E(m_\lambda)$ - soot absorption function.

The decay of the LII signal is related to the cooling time of particles and therefore to their size. Primary particle diameter can hence be determined, provided a model of the energy transfer during laser heating is available (Michelsen et al., 2007; Betrancourt et al., 2017). The LII technique has been continuously developed and optimized at University of Lille during the last decades (Bladh et al., 2006; Bejaoui et al., 2014). It has been applied to, e.g., the measurement of the soot volume fraction in turbulent flames (Lemaire et al., 2010) or in the exhaust of aero-engines (Delhay et al., 2009). Recent efforts were devoted to the detection of very small soot nanoparticles (Betrancourt et al., 2017, 2019). The LII technique was adapted here to probe soot particles in an optical cell mounted on the exhaust duct (Fig. 1), simultaneously

with PM collection for off-line analyses. The choice of the optimum cell location took into consideration the layout and space constraints of the test bed. Details of the LII experimental set-up are provided in the Supplementary Fig. S1. Briefly, LII measurements were performed with an excitation wavelength of 1064 nm generated by a Nd:YAG pulsed laser (Quantel Brilliant, 10 Hz repetition rate, 5 ns pulse duration). An optical attenuator is used to adjust the energy of the laser between 0 and 350 mJ/pulse. The excitation laser beam has a Gaussian profile and a diameter of 6 mm. A laser fluence of 0.32 J/cm^2 was used for excitation, thus maximizing the LII signal and limiting its dependence on laser fluctuations. The LII signal is collected by two achromatic lenses (f_1=200 mm, f_2=100 mm) and focused on the collection slit (100 mm x 0.2 mm). The signal, in the 400-825 nm spectral range, is then detected with a photomultiplier tube (PMT) (Hamamatsu R2257) and recorded by an oscilloscope (LeCroy 6050A, 500 MHz bandwidth, 5 GS/s sampling rate) triggered with a photodiode (Hamamatsu S1722-02). The PMT is equipped with a short-pass filter with a cut off at 825 nm. The performance of the set-up (with exactly the same geometry and collection volume) was priorly optimized and evaluated in the laboratory of Lille using carbon particles produced by a PALAS DNP 2000 generator. Set-points providing nearly constant particles concentrations could be obtained in the range 10^5 to $1.2 \cdot 10^6$ particles/cm^3. From these measurements a limit of detection of 10^4 particles/cm^3 was established.

2.3. Off-line characterization

2.3.1. Morphology and structure

For structural and morphological studies, particles collected on Au-coated or bare Si wafers are analyzed with Scanning Electron Microscopy (SEM) and Atomic Force Microscopy / Tip Enhanced Raman Spectrometry (AFM/TERS). The SEM Merlin (Zeiss) is used for the morphology analysis of collected particles; it features a spatial resolution of 1 nm and high detection efficiency. For the study of ultra-fine particles, a low accelerating voltage (1kV) was chosen to decrease the size of the interaction volume and improve the spatial resolution. Moreover, it enables the study of ultra-fine combustion-generated particles without the need of a conductive coating. Additionally, SEM images are used to determine the surface coverage and adjust, if needed, the sampling time.

The AFM (SMART SPM, HORIBA Scientific) features high-resolution cantilever-based tips (Hi'Res-C14/Cr-Au, μmasch, typical 1 nm-radius) for a high lateral resolution. A NanoRaman system that combines a SMART-SPM (HORIBA Scientific) with a Raman spectrometer (LabRAM HR Evolution Nano, HORIBA Scientific) is used for tip-enhanced Raman measurements (TERS). The system is based on a reflection configuration allowing the use of a 100x objective lens (NA 0.7) with a 60° angle. The incident laser (633 nm, p-polarized) is focused through the objective onto the apex of the cantilever-based silver TERS probe (Ag coated OMNI TERS probe). The collection of the back-scattered signal is performed through the same objective. The reliable stability of the whole system allows to maintain the laser-tip alignment and accurate XYZ position during the TERS map acquisition (at least 1 hour).

2.3.2. Chemical composition

Two-step laser mass spectrometry

Our group has extensively developed the two-step laser mass spectrometry (L2MS) technique over the last decade to specifically probe the chemical composition of combustion byproducts (Popovicheva et al., 2017; Delhaye et al., 2017; Faccinetto et al., 2011, 2015; Moldanová et al., 2009). The main advantages of L2MS are its high sensitivity and selectivity with regards to specific classes of compounds owing to the resonant ionization processes that can be adapted, by using different ionization wavelengths, thus targeting different classes of compounds and reaching sub-fmol limit of detection, *e.g.* for PAHs (Faccinetto et al., 2008, 2015). Systematic studies (Mihesan et al., 2006, 2008) have led to the optimization of the laser desorption process (and its coupling with the subsequent ionization step (Faccinetto et al., 2008), which ensures a soft removal (with minimum internal excess energy) of molecules adsorbed on the particle surface, and thus avoids/limits both their fragmentation and the in-depth damaging of the underlying carbon matrix (Faccinetto et al., 2015). In this work, a new mass spectrometer (Fasmatech S&T) is used, combining ion cooling, Radio Frequency (RF) guiding and Time of Flight (ToF) analyzer, which allows us to reach a mass resolution of

$m/\Delta m$ ~15 000. In this new experimental setup, the sample, placed under vacuum (10^{-8} mbar residual pressure), is irradiated at 30° angle of incidence by a frequency doubled Nd:YAG laser beam (Quantel Brilliant, λ_d= 532 nm, 4 ns pulse duration, 100 mJ cm^{-2} fluence, 10 Hz repetition rate) focused to a 0.07 mm^2 spot on the surface. The desorbed compounds form a gas plume expanding in the vacuum normally to the sample surface, and are ionized by an orthogonal UV laser beam (Quantel Brilliant, λ_i= 266 nm, 4 ns pulse duration, 10 Hz repetition rate, 0.3 J cm^{-2} fluence). At this ionization wavelength, a high sensitivity is achieved for PAHs through a resonance enhanced multiphoton ionization process 1+1 REMPI (Zimmermann et al., 2001; Haefliger and Zenobi, 1998; Thomson et al., 2007). The generated ions are then RF-guided to a He collision cell for thermalization and subsequently mass analyzed in a reflectron time of flight mass spectrometer (ToF-MS). A high sensitivity for aliphatic compounds was achieved with a similar instrument where the desorbed plume is ionized by a single photon ionization (SPI) process at λ_i=118 nm. The ninth harmonic of the Nd:YAG laser is generated in a coherent nanosecond source by frequency-tripling of a 355 nm pump beam (Continuum Surelite, 10 ns, 10 Hz) in a low-pressure Xe cell (Popovicheva et al., 2017).

Secondary Ion Mass Spectrometry

The particles were also analyzed with a commercial IONTOF TOF.SIMS^5 secondary ion mass spectrometer (SIMS) with maximum resolving power of $m/\Delta m$ ~10 000. The sample is placed on a holder and introduced into a vacuum chamber with residual pressure of ~10^{-7} mbar. The surface of the sample is probed by a Bi_3^+ pulsed ion beam at 25 keV. The primary ion source delivers a pulsed current of 0.3 pA. The penetration depth of the primary ions is typically 1-3 nm. In the static mode, used for the surface molecular analysis, the ion dose is limited to a level at which every primary ion should always hit a fresh area of the sample. A small fraction of the ejected atoms/molecules are ionized (secondary ions) and can thus be analyzed using a time of flight tube (V mode). Mass spectra are recorded in both positive and negative polarities, to obtain the maximum amount of information on the sample (Irimiea et al., 2018, 2019).

2.4. Theoretical model

The model-based workflow (Lee et al., 2019) simulates the in-cylinder gas phase and particulate produced in the engine and up to the sampling stage. There are two stages in the workflow: i) calibration of the in-cylinder pressure and engine-out emissions using a Stochastic Reactor Model (SRM), and ii) investigation on the formation of organic carbons in the sampling stage using a reactor network model.

SRM Engine Suite for in-cylinder combustion

The SRM is described by the probability density function (PDF) transport equation and it is assumed that the inhomogeneity is described by the distribution represented by the PDF everywhere. The multi-dimensional PDF transport equation is represented by an ensemble of N_{par} stochastic parcels. Each stochastic parcel is described by a collection of gas phase species mass fraction and a temperature, i.e.

$$(Y_1^{(i)}, \ldots, Y_{N_{\mathrm{S}}}^{(i)}, T^{(i)}) \tag{2}$$

where the superscript indices are labels for the parcels (up to N_{par}) and N_{S} is the number of species considered in the gas phase chemical mechanism. These quantities evolve through a number of processes, e.g. chemical reaction, turbulent mixing, flame propagation, wall impingement etc. (Bhave and Kraft, 2004; Etheridge et al., 2011; Smallbone et al., 2011; Lai et al., 2018). More detailed information on the application of the SRM in a GDI context can be found in Lee et al. (2019).

In addition to the gas phase composition and temperature, each parcel contains a particle population that consists of soot and inorganics. This model is directly coupled with the gas phase chemistry and a three-dimensional type-space is used to describe the particles:

$$P = (m, n_{\mathrm{prim}}, Y_{\mathrm{SOF}}) \tag{3}$$

where m is the particle's mass, n_{prim} is the number of primary particles and Y_{SOF} is the mass fraction of soluble organic fractions (SOF). The particle population evolves through inception from aromatics from the gas phase, surface growth, oxidation, and aggregation. The sectional method is used to solve the population balance model.

Reactor network model for the dilution stage

The engine-out composition, both gas and particulate phases, is passed onto a reactor network model to mimic the dilution process in the Dekati FPS 4000 diluter described in Section 2.1. The reactor network model is illustrated in Fig. 2. R1 and R3 represent the hot (180°C) and cold dilution (35°C) stages respectively, whereas R2 and R4 represent the piping connections. The model simulates a population of particles with the type space described by Eq. 3. From here, they can be post-processed to give particle size distributions, PN, PM and size-resolved SOF mass fractions. The outputs from the reactor network model are then compared with measurement data, which include particle size distributions and size-resolved chemical particle characterization.

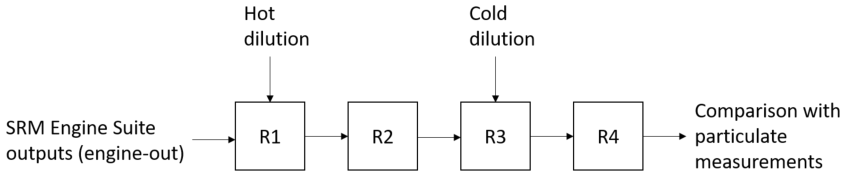

Figure 2: Reactor network model for the Dekati FPS 4000 diluter.

3. Results and Discussion

3.1. LII measurements within the exhaust duct

The LII technique was used in this work to monitor the evolution of the soot volume fraction (proportional with the LII peak signal, see section 2.2) upon various engine regimes. Fig. 3a shows the evolution of the LII signal (f_ν) with five engine set points. One can clearly see that the main parameter inducing a strong effect on the soot volume fraction is the timing of injection, leading to a 150-fold increase between the **NH** (270 deg. BTDC, see Table 2) and the **EI2** (311 deg. BTDC) regimes. This trend is correlated with the occurrence of pool fires (*i.e.* liquid fuel burning on the top of the piston) observed only for the points **EI1** and **EI2** using endoscopic imaging of the combustion chamber. This observation is consistent with the ones revealed by Velji et al. (2009) who experimentally identified that the main source of soot in the homogeneous combustion in a gasoline engine is due to the pool fires, while in the stratified mode the soot may also originate from local rich regions in the combustion chamber. Bardi et al. (2019) also observed a correlation between the occurrence of pool fires and the large increase in soot particle number. On the other hand, a moderate increase (by a factor of 3.2) is recorded when the indicated mean effective pressure (IMEP) quadruples, from 3 (**NS**) to 12 bar (**NH**). This is consistent with the work of Wang et al. (2014) who suggested that this trend could be due to slightly longer combustion duration for a clean injector.

In addition to the control of the soot volume fraction, time-resolved LII measurements can provide qualitative information about the size of the emitted particles. The LII signal time decays exhibit significant variations depending on the engine regime (see Fig. 3b). The "normal regimes" (**NS**, **NM**, **NH**) show similar decay times (*i.e.* relatively low influence of the IMEP on the particle size), whereas the non-optimal engine operation conditions (early injection, **EI1** and **EI2**) clearly show longer decay times *i.e.* larger primary particle sizes. The interpretation of these time-resolved LII decays in terms of soot primary particle diameter requires complex energy transfer modeling (Michelsen et al., 2007) which is beyond the scope of this work. This modeling is made even more difficult because size distributions of the particles are expected to be bimodal. Wang et al. (2014) measured on-line the size distributions of the particles in different GDI conditions by scanning mobility particle sizing (SMPS) and highlighted that most of the electrical mobility

diameter distributions were bimodal. Particularly they showed that the smallest nucleation mode particles could be prevalent in some engine conditions. Providing that LII modeling is undertaken, the coupling of LII with EEPS or SMPS offers promising perspectives. Indeed, in case of bimodality (which can be revealed by SMPS or EEPS), the LII could provide the diameter of the largest primary particles. The extraction of the primary particle diameter from the LII decays, even biased towards the largest ones, could give real-time access to this important characteristic without resorting to the use of off-line analyses (by e.g., TEM).

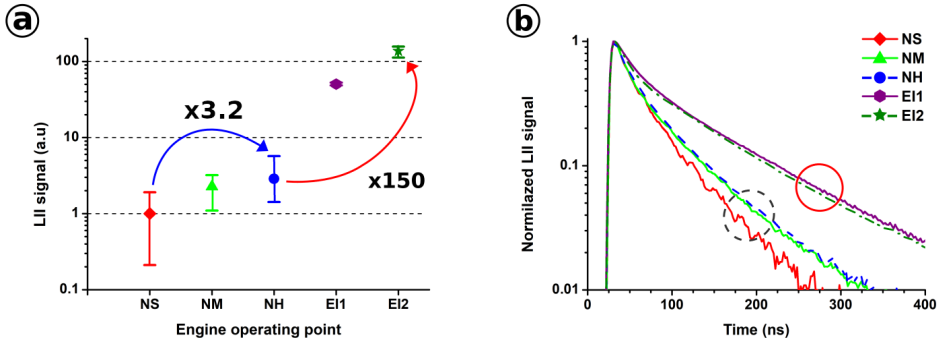

Figure 3: (a) LII peak signal (a.u.) measured at different engine set-points; (b) time-resolved LII signal.

These observations provide precious information for optimizing the simultaneous sampling of the particulates for off-line analyses. Further efforts will be devoted to calibrate f_ν using an extinction technique at a given engine set-point (Betrancourt et al., 2019) and to combine LII with particle sizers as mentioned above in a context of very small particles (down to 10 nm). From the LII measurements, several set-points showing a high stability have been selected for the off-line characterization, Table 2.

3.2. Structure and morphology

A significant challenge in collecting and studying combustion-generated particles is avoiding the agglomeration of the smallest ones during sampling. As small particles are the focus of this work, proper sampling is crucial to avoid the aggregation of small particles that would result in their collection on a different impaction stage (with a higher cut-off size compared to the dimensions prior to aggregation). Several samples of particles are analyzed with SEM, Fig. 4, in order to ensure that our experimental setup is able to sample and collect small primary particles. The particles are collected on Au-coated Si wafers with the Nano-DMA, set to a mobility diameter of 18 ±5 nm (see Section 2.1).

One can see that the samples (obtained in different engine regimes) contain predominantly single, spherical particles with a diameter ranging from 17 to 23 nm, Fig. 4, and are presumably primary soot particles. This is in agreement with previous studies on the emitted particles from GDI engines (Gaddam and Wal, 2013; Price et al., 2007). The fact that primary particles were successfully sampled indicates that the experimental setup is working as intended, minimizing the aggregation of particles to an extent that should not affect the subsequent chemical analysis.

AFM analysis is performed on samples collected in the **NH** engine regime (optimal conditions, high load), Table 2. The technique is used to determine the distribution and the size of single particles. AFM measurements are performed on a 1.2 x 1.2 μm region (300 x 300 pixels), Fig. 5a. The heights of particles 1 and 2 were determined to be 10 nm and 6 nm, Fig. 5d. The measured diameter is highly dependent on the used tip, especially when the radius of the scanned object is close to the one of the tip. The Full Width at Half Maximum (FWHM) diameters of particles 1 and 2, obtained with a sharp tip (r=1 nm), are <48 nm and <43 nm, respectively.

Two smaller zones have been characterized by TERS with a resolution of 7 nm/pixel (zone I) and 5 nm/pixel (zone II) and with a Raman integration time of 100 ms (one spectrum/pixel). The TERS maps of zones I and II are presented in Fig. 5b and 5c, respectively. Raman spectra of carbon materials contain two main features (see Fig. S2 in Supplementary Material): the G band, derived from in-plane motion of carbon atoms (around 1580 cm^{-1}) and the D band (D1), attributed to lattice motion away from the center

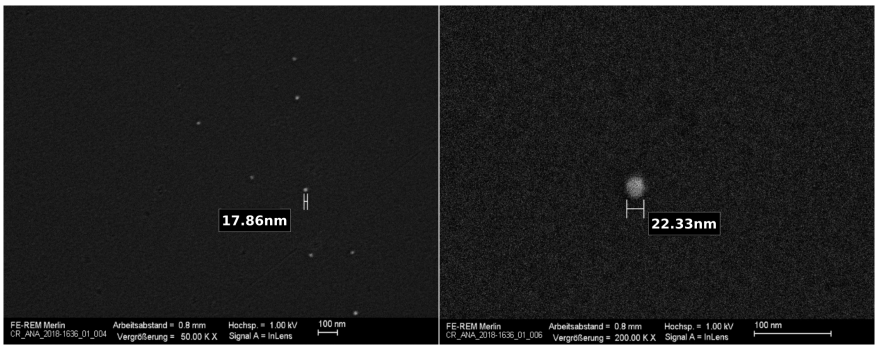

Figure 4: SEM images of size-selected particles (size bin centered at 18 nm) collected with a NAS in the **NH** (left panel) and **NM** (right panel) engine operating regimes.

of the Brillouin zone (around 1270 – 1450 cm^{-1}). The TERS maps displayed in Fig. 5b,c are obtained by integrating the G band only.

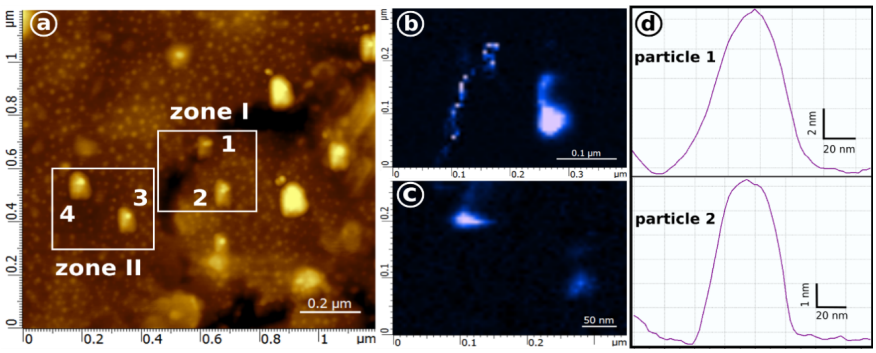

Figure 5: AFM and TERS study of nanoparticles collected in the **NH** engine regime (optimal conditions, high load). Topography image (1.2 x 1.2 μm) (a), TERS mapping of zone I, particles 1 and 2 (b), and zone II, particles 3 and 4 (c), topographic cross-section of particles 1 and 2 (d).

Besides TERS maps, TERS spectra were obtained for particles 2, 3, and 4 and are displayed in Fig. S2. The three spectra (Fig. S2) exhibit very different profiles (for example, the relative intensity of the D band to the G band is higher for particle 2 and lower for particles 3 and 4) which is indicative of major structural variations between particles collected in the same engine regime and the same size bin. A more quantitative approach involves a five-band fitting method, often applied to Raman spectra of soot particles (Sadezky et al., 2005; Parent et al., 2016), in which the G, D1, D2, and D4 bands are fitted with a Lorentzian profile, whereas the D4 band is fitted with a Gaussian profile. The fit results are presented in Fig. S2. The spectral parameters determined by curve fitting are highly variable across the three particles (Table S1), confirming our first observation. For instance, the ratio of the integrated areas of D1 to those of (G+D2) bands is usually considered as a good indicator of the order in the soot structure (Carpentier et al., 2012). This value increases from 1.5 (particle 4) to 2.5 (particle 3) and to 3 (particle 2), suggesting that particle 2 has a much more disordered structure compared to particles 3 and 4. In addition, the presence of strong signatures at 1208 and 1278.6 cm^{-1} on the spectra of particles 3 and 4 could be an indicator of organic molecules present on the surface of the particles.

These TERS measurements, performed (to the best of our knowledge) for the first time on ultra-fine combustion-generated particulate matter, reveal the diversity (at least in terms of nanostructure) of soot particles generated by the same engine, operating in the same conditions, and collected in the same size bin. This observation is of paramount importance for the interpretation of our off-line chemical composition measurements discussed in section 3.3, which, conversely, do not probe individual particles but rather a high number of them because of the diameter of the laser or ion beam used in the experiments. Therefore,

the properties and trends we derive in section 3.3 are averaged over many (different) particles making them statistically significant. These trends offer valuable input for the theoretical model, also operating with statistical approaches on particles ensembles.

3.3. Chemical characterization

To obtain a comprehensive chemical characterization and thus provide valuable inputs for building and validating the theoretical model, size-selected particles are analyzed with L2MS and SIMS. Data-treatment was performed according to our recently developed comprehensive methodology (Irimiea et al., 2018, 2019; Duca et al., 2019) which includes powerful statistical techniques such as PCA and HCA. Since the particles emitted in a certain engine regime are size-selected, a notation scheme that indicates the size of collected particles, in addition to the engine regime will be used from here forth (*<engine regime>:<upper size limit>-<lower size limit>*), *e.g.* **OM:180-100**. Due to a low particle coverage, the substrate (Al foil) was also probed which led to the formation of Al^+ and Al_2O^+ ions, detected at m/z 27 and 70, respectively. Consequently, even though the presence of Al compounds in such samples is typically a marker of engine wear, these peaks will rather be associated with the aluminum substrate in our case.

3.3.1. Size discrimination

One of the major points that need to be determined is whether the chemical composition of emitted particles varies with their size. On that ground, size-selected particles produced in two different engine regimes (**OM** – optimal conditions with an addition of oil, and **EM** – low air/fuel ratio) have been analyzed. These particular engine regimes were chosen as they simulate two completely different malfunctions, *i.e.* extreme cases of operation, equivalent to either a "worn out" engine with high oil consumption (**OM**) or a fault in the fuel system whith a normal oil consumption (**EM**). This information, along with similar analyses performed on size-selected particles emitted in other operation conditions, allows for a more precise calibration of the MGA.

*"Worn out" engine (**OM** regime)*

The analysis of samples obtained in the **OM** regime (optimal conditions, addition of oil) was performed with two-step laser mass spectrometry with two different ionization wavelength (266 nm and 118 nm), thus enabling us to selectively target either aromatic or aliphatic compounds. Several metals were detected (Na^+, K^+ and Ca^+) with both ionization wavelengths. While Na^+ and K^+ are mostly associated with fuel, they can also be present in the lubricating oil as trace elements (Huang et al., 1994; Cadle et al., 1997; Cross et al., 2012; Dallmann et al., 2014). In addition, the origin of Ca^+ is most likely the lubricating oil, since Ca is a component of detergent additives, widely used in modern motor oils (Cadle et al., 1997; Dallmann et al., 2014). Mostly aromatic species are detected when the ionization of laser-desorbed compounds is performed at 266 nm (Fig. 6). They are visually separated into two groups: one of lower and one of higher mass compounds. The first group is comprised of aromatic species with one to two aromatic rings and their alkylated derivatives (m/z 78 – 170) and is present in the spectra of all the samples with varying relative intensities. The second group is composed of aromatic compounds with three and more rings. According to Bari et al. (2010), the first group can be considered as volatile species, as they are mostly present in the gas phase. The second group is comprised of semi and non-volatile compounds. Therefore, the intensity ratio of the first to the second group is related to the overall volatility of the organic layer on the surface of particles. Species with masses between m/z 178 and 398 are detected on larger **OM** particles (180 – 32 nm), *i.e.* on samples **OM:180-100**, **OM:100-56**, and **OM:56-32**, while for the sample **OM:32-18** (32 – 18 nm) the highest detected mass is only m/z 278. Table S2 displays the assignment of the most intense mass peaks recorded by L2MS with two different ionization wavelengths (256 nm and 118 nm).

The intensity ratio of species belonging to the second group to those in the first one changes from sample to sample, within the **OM** regime. For the largest particles (**OM:180-100**) as well as for the smallest (**OM:32-18**), the first group ($78 \leq m/z \leq 170$) shows a higher intensity. However, for samples **OM:100-56** and **OM:56-32**, the second group ($m/z \geq 178$) exhibits a higher contribution. Within the first group, for all the samples the base peak is located at m/z 128 and the group features fairly constant peak and intensity

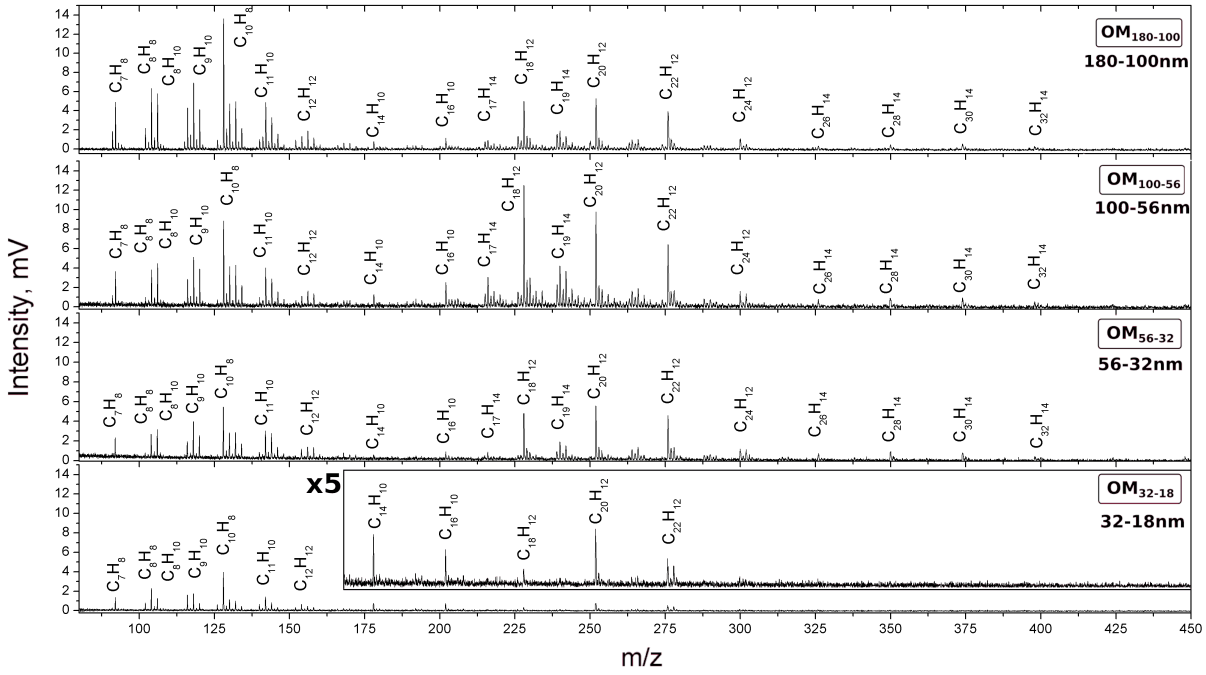

Figure 6: L2MS spectra of four samples (particle size 180-18 nm) obtained in the **OM** engine conditions (optimal operation, medium load). The analyses were performed with an ionization wavelength λ_i=266 nm to target aromatic compounds.
New figure

distributions. The second aromatic group shows a distinct behavior, where the base peak is m/z 252 for samples **OM:180-100**, **OM:56-32**, and **OM:32-18**, but m/z 228 for sample **OM:100-56**. However, with the exception of the peak at m/z 228, peak and intensity distributions change only slightly from sample to sample. The change in the relative intensity of the m/z 228 peak is probably linked to a $C_{18}H_{12}^+$ isomer present on particles in the size range 100 – 32 nm. The fact that only species up to m/z 278 can be seen on sample **OM:32-18** might be explained by an overall lower intensity, as this sample had the lowest coverage of deposited particles. However, since the contribution from the highest masses (*e.g.* $m/z \geq 275$) does not exceed a few percent of that given by the whole distribution of aromatic compounds making up the second group ($\geq$ 3-ring aromatic compounds), we can still derive the intensity ratio of species from the second group to those belonging to the first one. A low ratio observed for this sample suggests that smaller particles contain mostly light aromatic species.

The samples also contain a variety of aliphatic species, detected with a different ionization scheme (λ_i=118nm)(Popovicheva et al., 2017), Fig. S3. Ion series with the formula $C_nH_{2n-1}^+$ is typical of cycloalkanes and alkenes while the $C_nH_{2n+1}^+$ series (alkyl fragments) is typical of linear or branched alkane compounds (McLafferty and Tureek, 1993). The series at m/z 67, 81, 95, and 109 (C_nH_{2n-3} fragments of bicycloalkanes) is also present, however with a very low intensity. The asymmetrical shape of the peaks is a sign of fragmentation. The fragmentation pattern is characteristic of the presence of aliphatic hydrocarbons, alkanes (C_nH_{2n+2}). As alkane cations are not stable, especially if the excess internal energy is high after ionization, they can easily fragment. Since lubricating oils tend to be dominated by cycloalkanes due to the deliberate removal of *n*-alkanes during a de-waxing process (Tobias et al., 2001), an intense signal for cycloalkanes is usually a sign of oil contribution. The main source of aliphatic compounds can be derived from the ratio of n-alkanes to cycloalkanes. The signal corresponding to alkanes is superior to that of neighboring cycloalkanes in the mass range m/z = 67 – 71 and 81 – 85 when the fuel is the main source of these compounds, and inferior for the lubricating oil (Dallmann et al., 2014; Sakurai et al., 2003; Tobias et al., 2001). Ion signals at m/z 71 and 85 are lower than signals at m/z 69 and 83, suggesting that the measured exhaust particles mainly consist of unburnt lubricating oil (in case of diesel particles this pattern

would be caused by at least 95% oil and 5% fuel, while in the case of gasoline, the ratio should be higher (Dallmann et al., 2014; Sakurai et al., 2003). The one exception is observed for the sample **OM:100-56** where the signal at m/z 69 is lower than that of m/z 71 (r = S_{69}/S_{71} ≈0.8), while the m/z 83 to 85 ratio is close to unity. Since the source of organic species in the exhaust includes fuel, lubricating oil, and their partially oxidized products, it is possible that particles containing the most unburnt fuel are concentrated in the size bin associated with sample **OM:100-56** (100 – 56 nm) and decreases towards both smaller and larger particles. Peaks at m/z 50, 64, 66 and 78 can be attributed to fragments of aromatic species. Series of highly unsaturated aliphatic compounds are present as well: $C_{2n}H_2^+$ and $C_{2n}H_4^+$. These series were attributed to polyynic fragments, known to be present in rich premixed flames and play an important role in the formation of combustion-generated particles (Hansen et al., 2008; Li et al., 2009).

To classify the samples and uncover differences and similarities between them, principal component analysis (PCA) was used (Irimiea et al., 2018, 2019; Duca et al., 2019). This statistical method is able to reduce the number of dimensions of complex mass-spectrometric data, thus increasing its readability, while still preserving most of the original information. Before applying PCA, the data was first normalized and baseline corrected (Irimiea et al., 2018, 2019; Duca et al., 2019) while all peaks associated with the substrate were disregarded. Each principal component (PC) accounts for a defined percentage of the variance within the dataset. For both ionization schemes, the first two components are responsible for most of the variation between samples (containing particles of different sizes) (≈ 97 %), and therefore the number of dimensions of the original data was reduced to only two. The contribution of mass peaks to each principal component is represented by their loading (Fig. S4), which reflects the interpretation of individual components. To extract the maximum amount of information, the data obtained with different ionization wavelengths was treated separately. In case of the ionization at 266 nm, the first principal component (PC1) can be associated with the total number of different aromatic species, since it receives a high negative contribution from both alkylated and non-alkylated PAHs. The first group of aromatic compounds ($78 \leq m/z \leq 170$) shows a high positive contribution to the second principal component (PC2) while the second group ($m/z \geq 178$) is related to the negative PC2 value. For the data obtained with 118 nm ionization, PC1 is linked to all detected aliphatic species and can be also seen as an indicator of the homogeneity of aliphatic signal throughout the mass spectrum. PC2 has a strong contribution from highly unsaturated hydrocarbons ($C_{2n}H_2^+$, $C_{2n}H_4^+$, positive PC2) and several aliphatic species (negative PC2), Fig. S4. Moreover, since contributions to PC2 from $C_{2n}H_2^+$, $C_{2n}H_4^+$, and aliphatic species ($C_nH_{2n-1}^+$, $C_nH_{2n}^+$, $C_nH_{2n+1}^+$) have the opposite sign, PC2 represents the ratio of highly unsaturated hydrocarbons to aliphatic species. In addition, the fact that peaks at m/z 50, 52, 74 and 78 (fragments of aromatic species) have a high contribution to PC2 proves that these species have the same origin, which is in agreement with soot formation models (Hansen et al., 2008; Li et al., 2009).

Data in terms of PC1 and PC2 for both ionization wavelengths are presented in Fig. 7. There is a notable separation between different samples, thus demonstrating the capability of the PCA method to discriminate between samples that present, at first glance, similar mass spectra. Data points for each sample are clustered together, proving that the sample surface is homogeneous and the reproducibility of the method is high. Sample **OM:180-100** contains a large number of aromatic species (266 nm ionization), with a higher contribution coming from the light-weight compounds ($78 \leq m/z \leq 170$). In contrast, sample **OM:100-56** exhibits a higher contribution from the second group of aromatic compounds ($m/z \geq 178$). Sample **OM:56-32** seems to have fewer species, however heavier compounds ($m/z \geq 178$) still dominate. For the smallest analyzed particles, *i.e.* sample **OM:32-18**, the contribution of lighter aromatic compounds increases considerably, with only a few species detected from the second group. It appears that aromatic species with a lower mass are present on all samples and are not bound to a specific particle size. In contrast, there is a clear increase in the contribution from higher mass aromatic species for **OM:100-56** and **OM:56-32** samples, suggesting that these compounds preferably adsorb on particles in this size range (100 – 32 nm). Sample **OM:100-56** shows the most peaks coming from aliphatic species (118 nm ionization), including peaks in the mass range m/z 64 – 112 (which reflects as a negative PC1, the latter being representative of all detected aliphatic species in Fig. 7). The smallest number of aliphatic compounds were detected on the **OM:56-32** sample which also has a fairly inhomogeneous-looking spectrum (Fig. S3). The contribution of highly unsaturated hydrocarbons ($C_nH_2^+$ and $C_nH_4^+$) decreases with the size of particles, being the highest

for the **OM:32-18** sample and the lowest for the **OM:180-100**, positive PC2. At the same time, the contribution of other aliphatic compounds increases with the particle size.

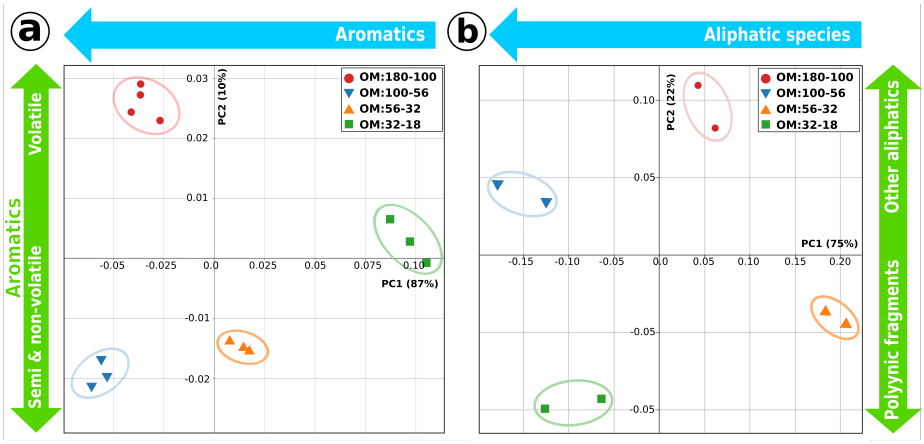

Figure 7: Size separation of combustion-generated particles obtained in the **OM** engine regime (optimal operation with addition of oil, medium load) by means of principal component analysis, with ionization wavelengths of λ_i=266 nm (a), or λ_i=118 nm (b). Species were classified as volatile, semi- and non-volatile compounds according to Bari et al. (2010).

*Fuel system failure (**EM** regime)*

Another engine regime that simulates a malfunction is **EM** (low air/fuel ratio, medium load), which acts as one more extreme operation point, this time with a normal oil consumption. Particle emissions obtained in this engine regime are analyzed with SIMS in both positive and negative polarity (Fig. S5 and Fig. S6, Table S3 contains all the detected peaks in both polarities). Metallic and metalloid ions such as Na^+, Mg^+, Al^+, Si^+, K^+, Ca^+ and Cu^+ are present, however, their intensity is higher for the blank aluminum foil, and therefore they will be assumed to be coming from the underlying substrate rather than from the collected particles. All spectra obtained in the positive polarity are dominated by hydrocarbon fragments $C_nH_m^+$. Masses between m/z 128 and 300 can be mostly attributed to PAHs. Additional minor signals correspond to NH_4^+ and oxygenated species such as CH_3O^+ (m/z 31), $C_2H_4O_2^+$ (m/z 60) and CHO_4^+ (m/z 77). CH_3O^+ can be associated with methyl esters or ethers. Alternatively, it can correspond to primary alcohols or methyl-carbinols. The oxygenated positive ions, CH_3O^+ and $C_2H_4O_2^+$ present the highest correlation (R = 0.98) between the integrated areas of their peaks (normalized with respect to total ion count, TIC), thus indicating a common source. For instance, isopropanol, which is used as a gas dryer additive in gasoline for fuel system protection (Patil et al., 2014), could be a common source for these two ions. Ferrocene ($Fe(C_5H_5)_2$) is believed to be present in the fuel, since its fragment ($FeC_5H_5^+$) was detected. Ferrocene is sometimes used as a fuel additive that acts as an antiknock agent. Hopanes and n-alkanes (C_{26} – C_{36}) were also detected, they are believed to be linked to unburned lubricant oil (Wang et al., 2009). The high correlation between these peaks (R = 0.85 – 0.98) also suggests a common source. The correlation between PAHs and hopanes is almost non-existent, therefore we can conclude that PAHs are formed during the combustion process and are not remnants of oil/fuel. Negative SIMS spectra, as presented in Fig. S6, are dominated by H^-, O^-, and OH^- fragments. Additional strong features correspond to the C_n^- and C_nH^- (n = 1 – 9) series with the hydrogenated carbon cluster C_nH^- being more intense compared to C_n^- when n is an even number (except in the case of n = 1). C_n^- (n = 2 – 4) fragments are considered to be a marker for elemental carbon (EC) in aerosol mass spectrometry (AMS) data (Pagels et al., 2013). The fact that detected carbon clusters have the same source is confirmed by the high positive correlation factors between C_2^-, C_3^-, and C_4^-. The correlation between C_3^- and C_4^- is the highest (R_{max} = 0.95), while the lowest is between C_2^- and C_4^- (R_{min} = 0.74).

All samples can be easily separated by PCA, Fig. S7, and by hierarchical clustering analysis (HCA), Fig. 8. For the PCA, the first two principal components account for 92% and 95% of the total variation

within the data obtained in the positive and negative polarity, respectively. For the positive polarity, the first principal component receives a high negative contribution from aliphatic compounds ($C_nH^+_{2n-1}$ and $C_nH^+_{2n+1}$, negative PC1), while other aliphatic species show a positive contribution. PC2 can be seen as the ratio of aliphatic species (positive PC2) to aromatic compounds, such as PAHs and their fragments (negative PC2 value). For the negative polarity, PC1 is related to the ratio of the amount of oxygenated species to the C_n^-, C_nH^- family (with a positive PC1 contribution linked to a high fraction of oxygenated species while a negative PC1 value indicates a high amount of C_n^-, C_nH^-, *i.e.* a high EC). PC2 is linked to oxygenated species (positive for hydrocarbon-based compounds and negative for oxygenated species containing S, P and N). From Fig. S7, it is clear that PCA can easily distinguish between samples, implying that size-selected particulates are also chemically different in the **EM** regime. It clearly shows that aliphatic species are concentrated predominantly on samples **EM:180-100**, **EM:56-32**, and **EM:32-18** and that aromatic compounds are present in comparable amounts on the lower four stages, 100 – 10 nm particle size (**EM:100-56, EM:56-32, EM:32-18** and **EM:18-10**). Samples **EM:100-56**, **EM:56-32**, and **EM:32-18** (100 – 18 nm size range) exhibit the highest amount of C_n^- and C_nH^- ions, and therefore have a high EC content. Sample **EM:180-100** has the highest contribution from oxygenated compounds that contain elements other than carbon and hydrogen (*e.g.* PO_3^-, SO_3^-, SO_4^-, PO_4^-, $NaSO_4^-$), while samples **EM:100-56** and **EM:18-10** contain the lowest. Eventually, negative polarity SIMS data extracted from **EM** samples (Fig. S7) can be divided into three main clusters according to the amount and nature of oxygenated species present on the samples. Specifically, the first cluster encompasses the two samples which exhibit the most oxygenated species, *i.e.* **EM:100-56** and **EM:18-10**. The second cluster gathers the two samples which bear much less oxygenated species compared to the others, along with more elemental carbon, *i.e.* **EM:56-32** and **EM:32-18**. Lastly, the third cluster is sample **EM:18-10**, which contains the most inorganic oxygenated species of all samples.

HCA is a statistical technique able to group samples according to the distance between them in a multidimensional space while also accounting for the total variance within the dataset (Rencher, 2000; Pei et al., 2008). The distances between the samples are represented in form of a dendogram, Fig. 8. We can see that samples **EM:180-100, EM: 56-32**, and **EM:32-18** form a relatively small cluster (small distance between data-points), thus indicating their similarity. Likewise, **EM:100-56** and **EM:18-10** samples are grouped together hence forming a second cluster, well separated from the first one. Samples in these two clusters are thus very different, primarily due to the high contribution of $C_nH^+_{2n-1}$ and $C_nH^+_{2n+1}$ ions to **EM:100-56**, and **EM:18-10** samples (as already shown by PCA). Interestingly, the distance between the blank and the second cluster (**EM:100-56** and **EM:18-10** samples) is relatively small, which can be explained by the lower coverage of these samples.

3.3.2. Source discrimination

We showed in section 3.3.1 that some chemical compounds of different provenience are preferentially found on particles featuring a distinct size range. It is now possible to determine the contribution of major sources to the formation of particulates. Determining the impact of various sources to the chemical composition of particulates will help further improve the theoretical model. On that basis, samples obtained in engine operation regimes (**OM**, **EM**, **NM**, and **NH**) with different contribution from fuel and oil (main sources of particulates) are analyzed and compared using PCA.

The first two PCA components, PC1 and PC2 (∼98%) are presented in Fig. 9. It is clear that particles produced in an optimized engine regime (medium and high load) are chemically very different from the ones produced in non-optimal ones and, therefore, can be easily separated by their principal components (Fig. 9a). PC1 alone (∼91%) allows the separation of regimes, based on the abundance of aliphatic fragments (positive contribution to PC1, Fig. S9). Consequently, samples produced in non-optimal regimes are characterized by a higher relative contribution from aliphatic fragment ions compared to optimized engine regimes. PC2 is linked to the aliphatic fragment ions and aromatic species (positive PC2 value), however some aliphatic fragment ions ($C_5H_7^+$, $C_5H_9^+$, $C_3H_7^+$, $C_4H_7^+$) contribute to the negative value of PC2. Data points corresponding to optimal engine regimes form a smaller cluster, implying that particles produced in non-optimal conditions exhibit a much larger variability in their chemical composition.

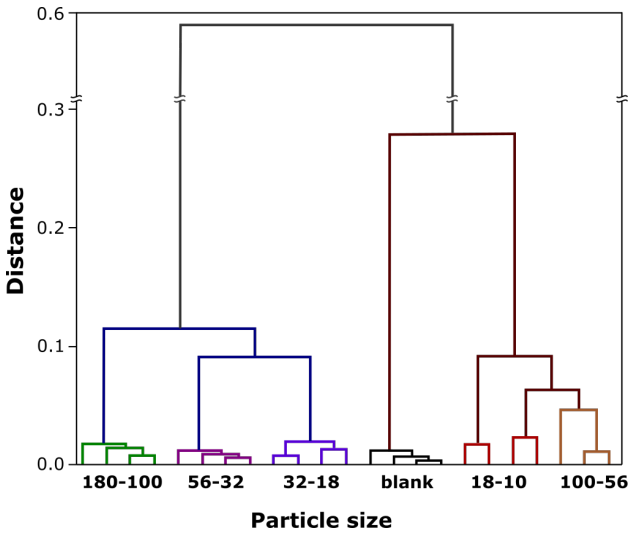

Figure 8: Separation of size-selected particulates obtained in the **EM** (low air/fuel ratio) engine regime by the hierarchical clustering analysis based on positive polarity SIMS spectra.

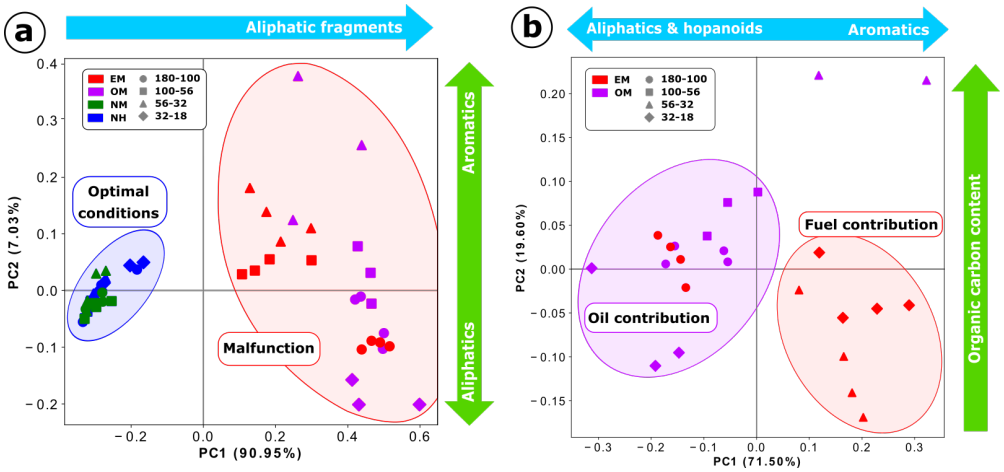

Figure 9: Separation between different engine regimes (a) and main sources of particles (b).

The two non-optimal regimes have been compared using the same statistical method, which further enables the distinction between the two main contributors to particulate emissions from the internal combustion engine: fuel and oil, Fig. 9b. PC1 (∼71%), which is accountable for the separation of the two regimes (and consequently sources), is linked to the contribution of hydrogen-rich hydrocarbons on one side (negative contribution) and to fragment ions and aromatic species on the other (positive contribution, Fig. S9). This reveals that oil-related particles feature more hydrogen-rich hydrocarbons, while an excess of gasoline leads to the production of more aromatic species. The increase in the contribution of fragment ions in the latter is probably linked to the increase in the aromatic contribution, since the majority of fragments can be associated to the fragmentation of PAHs (McLafferty and Tureek, 1993). PC2 (∼20%) is associated with the presence of aromatic hydrocarbons, thus confirming that the presence of aromatic species is related to fuel combustion. Two data-points, corresponding to **OM:56-32**, show a rather high contribution from OC, and aromatic compounds in particular, unlike other **OM** samples. Since these compounds are linked to the contribution of fuel, we can infer that, for the **OM** regime, particles in this size (56-32nm) mostly originate from fuel combustion.

3.3.3. Influence of the catalytic stripper

We have previously shown the analysis of collected particles from the "raw exhaust" (at the exhaust port), and thus gathered information about the chemical composition of emitted particles that will serve as inputs to test and improve the MGA. However, particles present in the "raw exhaust" contain a multitude of organic species (as is shown above), with various degrees of volatility, and since the current regulations limit only the number of non-volatile particles, one should also study PN emissions after the removal of the volatile fraction. This is especially important in this study as this information will also help characterize and model the catalytic stripper (CS) that will be used to remove volatile compounds in the PEMS measuring system – whose development is the ultimate goal of the PEMS4Nano project. For such a system, volatile removal efficiency of the CS should be in accordance with European regulations, that is to say >99% removal of $\geq$ 30 nm tetracontane (CH_3–$(CH_2)_{38}$–CH_3) particles with an inlet concentration of $\geq$10000 cm^{-3} at the minimum dilution (European commision, 2017). However, supplementary efforts are currently being made to better understand how the CS that complies with these regulations affects other individual organic compounds that are commonly present on the surface of combustion generated particles (such as PAHs) – important information for modeling the non-volatile fraction leaving the CS and entering the counting stage of the instrument. To study the influence of the CS, two sets of exhaust particles are collected and subsequently analyzed. One set was sampled with and one without the catalytic stripper. The engine regime was exactly the same for both sets of samples. Here we only show some preliminary results on the influence of the CS to the chemical composition of emitted particles, however, a more complete and detailed study will be presented in an upcoming paper.

From the mass spectra (L2MS) of the two sets we can already see the difference in the absolute intensity of all the peaks corresponding to organic species (considerably smaller for the samples obtained with the catalytic stripper). However, the signal which corresponds to carbon clusters is considerably higher for particulates sampled after the catalytic stripper (Fig. S10). PCA clearly shows that particles sampled with and without the catalytic stripper can be discriminated based on their OC and EC content (PC1). The second principal component is linked to the the organic fraction and small mass carbon clusters (C_{10}^+ and C_{11}^+, positive PC2 value) as well as the contribution from carbon clusters with a higher mass (negative PC2 value), Fig. S11. The catalytic stripper removed the volatile particles as well as the organic species from the nonvolatile core and, as a result, the contribution of EC (carbon clusters) increased, Fig. 10. Accordingly, particles present in the "raw exhaust" have a higher contribution from organic components, Fig. S11. The only exception are the particles in the size range 56-18 nm (**NHC:56-32** and **NHC:32-18**), which might be the result of a combination of (i) a high contribution from organic components to particles in this size-range (as previously shown), and (ii) a lower efficiency of the catalytic stripper in this size-range (Swanson et al., 2013).

Generally, particles sampled with a catalytic stripper are characterized by a weak contribution from organic species and a much high elemental carbon content (linked to the presence of carbon clusters, C_n). From the above preliminary results we can conclude on the effectiveness of the catalytic stripper in removing most of the organic fraction from the surface of the particles.

3.3.4. Trends in the chemical composition

A detailed chemical characterization of particulate matter is desirable and can elucidate the soot formation, growth, ageing, and reactivity. However, to facilitate the comparison of mass spectrometric results with other experimental measurements and also support the interaction with modelers that use the data as inputs for various scale simulations, individual compounds are often grouped into classes. Compounds are grouped based on their chemical family (aromatics$^+$, $C_nH_{2n-1}^+$, $C_nH_{2n-3}^+$, hopanes$^+$, n-alkanes$^+$) as well as their connection to the elemental carbon content ($C_n{}^-$)(Gilardoni et al., 2007; Kirchner et al., 2003). Moreover, OC can be expressed as the sum of the former groups of organic compounds (Pagels et al., 2013; Delhaye et al., 2017). These chemical families/groups have been chosen as they have different sources and roles in the formation and ageing mechanism of combustion-generated particles (*e.g.* PAHs are associated with the combustion of gasoline, while hopanoid compounds are seen as markers of unburnt lubricating oil). The contribution of a group to a mass spectrum is equal to its normalized intensity (to TIC). As an example, trends in the chemical composition for the **EM** engine regime are illustrated in Fig. 11, where

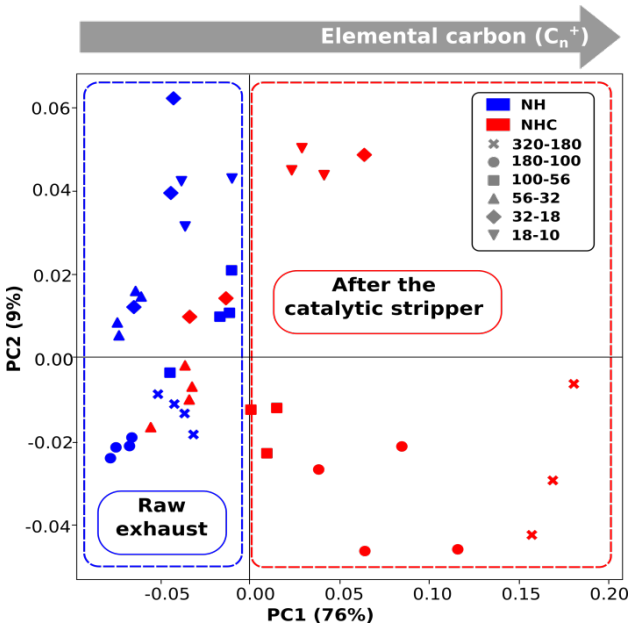

Figure 10: Discrimination between particles sampled from the raw exhaust and after the catalytic stripper.

the error bars correspond to the standard deviation associated with multiple zones of each sample. The normalized signals obtained for the blank filter are given for comparison. For most of the fragments, relative intensities of the blank filter are negligible. The total contribution of aromatic compounds and the C_n^- family increases towards sample **EM:32-18**; a similar variation was also found for **NM** and **HM** engine regimes. Aliphatic families ($C_nH_{2n-1}^+$ and $C_nH_{2n-3}^+$) are the most abundant on samples **EM:180-100**, **EM:56-32** and **EM:32-18**, when only a small contribution is observed for the other two samples (peak intensities comparable to those of the blank aluminum foil). Hopanes and n-alkanes are mostly present on sample **EM:180-100** and since they are attributed to the lubricating oil, one can conclude that the unburnt oil is found predominantly on bigger particles. This is slightly different compared to the **OM** engine regime where the oil contribution is the highest on sample **OM:100-56**. This difference might be linked to the state of the oil in the combustion chamber: for the **EM** regime, the oil originates from an oil film present on the cylinder liner while for **OM** regime, oil was deliberately added to the combustion chamber, forming a mist.

The relative abundance of the C_n^- fragments (markers of the elemental carbon), compared to the TIC in the negative polarity SIMS spectra is shown in Fig. 11. The relative proportion of these fragments increases from the sample made of the largest particles (180-100 nm) to that holding the smallest ones, reaching its maximum for sample **EM:32-18** and then dropping significantly for **EM:18-10**. Fig. 11 shows, once again, that the chemical composition of emitted particles changes with their size because of a size-dependent contribution from different sources of particle emission (*e.g.* fuel/oil combustion, unburnt oil).

3.4. Simulation results

Computational combustion modeling is an essential, complementary tool to engine experiments (Pitz et al., 2007). Detailed soot models use extensive chemical mechanisms consisting of hundreds of chemical reactions and detailed particle dynamics to predict the formation of soot particles. These kinds of models are able to provide a deep insight into the soot formation and oxidation mechanism (Kong et al., 1995; Hong et al., 2005; Pitz et al., 2007; Wu et al., 2019a,b). They provide the opportunity to efficiently optimize the performance of internal combustion engines, allowing to represent the combustion of fuel in a variety of practical devices (*e.g.* spark ignition direct injection engines). An essential component of such models is the availability of extensive experimental data, for both fuel and combustion by-products, of sufficient quality to

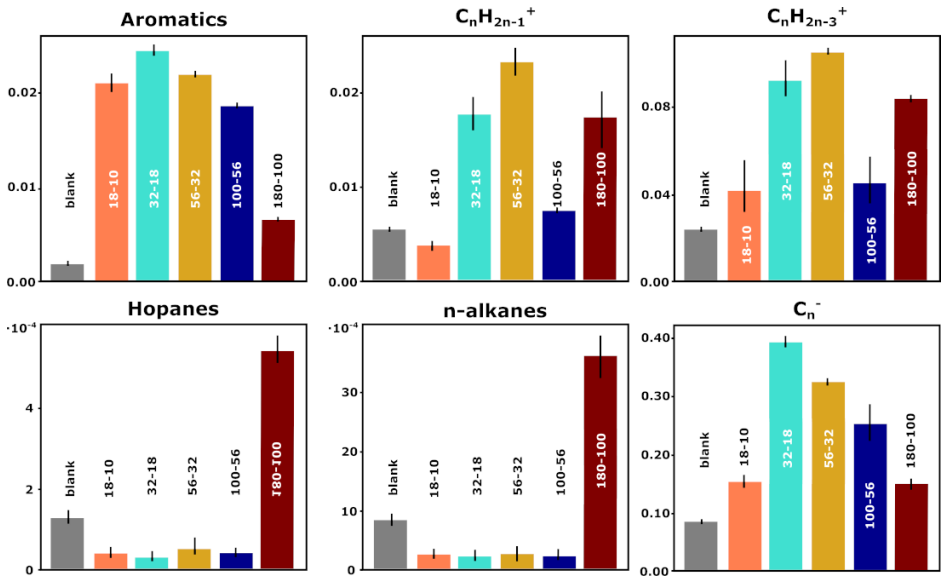

Figure 11: Integrated peak areas of positive and negative SIMS fragment ions of interest normalized to the total ion count (TIC) for particles produced in the **EM** engine regime (low air/fuel ratio). The error bars represent the standard deviation among all analyzed zones.

first identify important species that need to be included in the model and then validate it. The information about the OC and EC content presented here was used to validate the model guided application (Lee et al., 2019) utilized in the development and optimization of the particle number emission monitoring systems for particulates down to 10 nm. Other findings (*e.g.* the size-dependent contribution of hopanoid species or aliphatic compounds) can be subsequently used in the development of additional theoretical models, for instance dedicated to assess the contribution of lubricating oil to particle emissions.

The SRM Engine Suite was first applied to model 12 steady state operating conditions of the gasoline direct injection single-cylinder test engine. Experimentally obtained in-cylinder pressure profiles, gas phase emissions (*e.g.* CO, μHC, NO_x), particle concentrations and size distributions have been used to calibrate the model. Additionally, size-resolved chemical composition was employed for its validation. Due to the involved complexities, only one representative point is used here to compare with chemical characterization results.

In-cylinder pressure profiles obtained experimentally showed good agreement with the outputs of the model and hence ensure that the combustion behavior is modeled accurately, Fig. S12. This is essential because the particulate phase is directly coupled to the gas phase and detailed mechanisms are used for both phases. In order to produce soot in the particulate phase, the necessary precursors need to be present in the gas phase and this is only possible if the combustion characteristics are captured correctly. A similar agreement can be observed for the particle number (Fig. 12a) and size distributions, shown for several selected operating points (Fig. 12b). In Fig 12, it can be observed that the simulated particle size distributions tend to fit the larger size ranges poorly. This is acceptable as the experimental results also show larger errors for the large particles. Besides that, this project is focused on the smaller particles around 10 nm, therefore it is more important to simulate the formation of the smaller particles more accurately. It is also worth mentioning that the particle size distributions have a peak around the 10 nm region and because of this, the model calibration is weighted towards the smaller sizes. The peaks are not obvious in the plots because the axes are logarithmically scaled.

The particle populations are then further used to calculate the SOF mass fraction and layer thickness (Fig. 13) as well as the number of primary particles per aggregate and their size (Fig. S13). These results allow for a comparison with experimental data obtained by off-line chemical characterization (*e.g.* organic carbon content) and SEM measurements, respectively. Fig. 13 demonstrates a sensitivity analysis of the

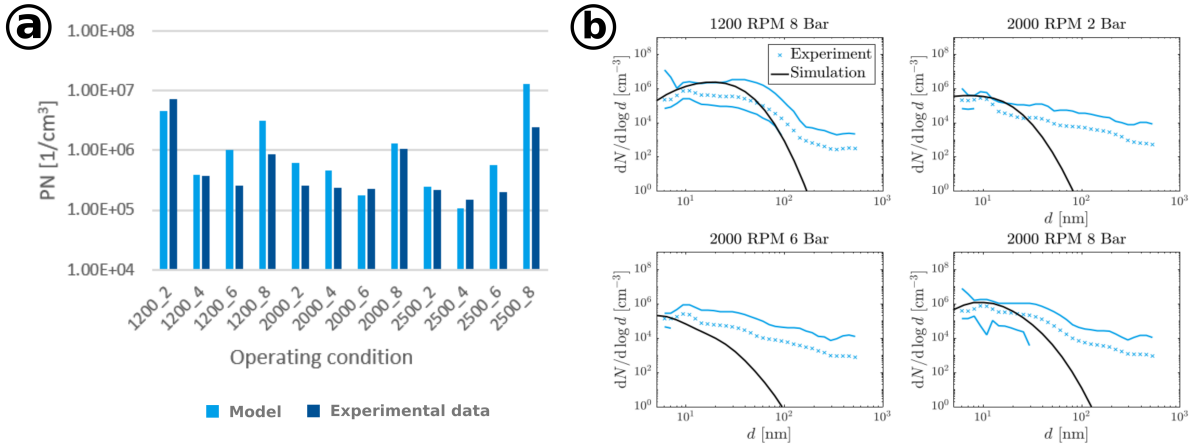

Figure 12: **(a)** – Calibrated PN for all studied operating points, **(b)** – Particle size distributions for a selection of operating points. The dashed lines represent the upper and lower bounds from the measurement data. Due to logarithmic scaling of the axes, some lower bounds with the value zero cannot be plotted.

effects of engine load on the formation of SOF on the particles. From the perspective of the chemical characterization of the particles, the model is validated by comparing the SOF layer thickness with the experimentally measured OC content (Section 3.3.4). The bump in the SOF layer thickness observed in the measurements was mimicked well by the model. In this paper, only qualitative comparison is made between the simulated and measured results from an operating point. The simulated results show that the quantity of SOF is a strong function of the engine operating condition. Data from different operating conditions are required to further validate and improve the model. The measurements and the model results also confirmed that surface composition is not a measure of bulk characteristics. Based on the simulated results, the SOF mass fraction shows a different trend compared to the SOF layer thickness. Lastly, the calculated primary particle sizes as a function of aggregate size can be compared against results generated from SEM images (e.g. Fig. 4) when more measurements become available in the future.

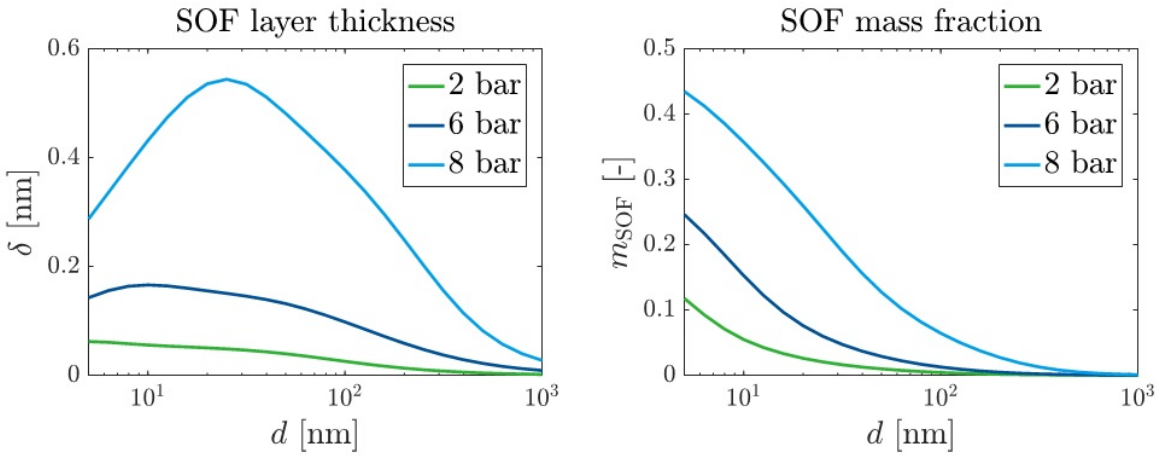

Figure 13: Sensitivity of SOF layer thickness and mass fraction with engine load. Engine speed is held constant at 2000 RPM.

Conclusions

Particles emitted by a gasoline single cylinder direct injection engine have been characterized by a combination of on-line and off-line techniques enabling extensive information to be gathered relative to the

structure, morphology and composition of the particulate matter, and their variation with particle size. Detailed molecular-level characterization of size-selected particles by mass spectrometric techniques coupled with statistical procedures showed decisive evidence for the variation of the chemical composition with particle size. Moreover, identification of key chemical markers allowed clear discrimination of particles by source (fuel, lubricant, engine wear) and engine operating regime. It was also shown that a catalytic stripper that complies with European regulations for PMP systems (>99 % removal of $\geq$ 30 nm tetracontane) successfully removes the majority of particle-bound organic species. Atomic force and scanning electron microscopies were used to monitor the morphology of the collected particles, while Tip-Enhanced Raman Spectroscopy was used for the first time to probe the nanostructure of sub-10nm combustion-generated particles. The latter showed that ultrafine particles that are produced and collected in the same engine regime can be still very different.

Model Guided Application comprising physico-chemical simulation and advanced statistics has been formulated as part of the development of PEMS methodology to support the understanding of the formation and evolution of the particles in the engine up to the measurement sampling line. The results demonstrate the ability to use a model-based framework to assess the performance of an experimental setup. The particle measurements ranging from particle number concentrations, particle size distributions and chemical composition are essential to calibrate and validate the detailed physico-chemical model presented in this paper. It is important to note that such measurement data is highly relevant for improving the fidelity of a variety of modeling approaches, ranging from 0D, 1D engine cycle, to 3D computational fluid dynamics, particularly, given the poor predictive capability of simulation tools for particulate emissions. The modeling work presented in this paper is related to a single-cylinder test engine, and is also directly applicable to multi-cylinder engines as well as at vehicle level.

Acknowledgements

This project has received funding from the European Union's Horizon 2020 research and innovation programme under Grant Agreement no. 724145.

References

An, Y.Z., Teng, S.P., Pei, Y.Q., Qin, J., Li, X., Zhao, H., 2016. An experimental study of polycyclic aromatic hydrocarbons and soot emissions from a GDI engine fueled with commercial gasoline. Fuel 164, 160–171. doi:10.1016/j.fuel.2015.10.007.

Atkinson, R.W., Fuller, G.W., Anderson, H.R., Harrison, R.M., Armstrong, B., 2010. Urban ambient particle metrics and health: a time-series analysis. Epidemiology , 501–511doi:10.1097/EDE.0b013e3181debc88.

Bachalo, W.D., Sankar, S.V., Smallwood, G.J., Snelling, D.R., 2002. Development of the Laser-Induced Incandescence Method for the Reliable Characterization of Particulate Emissions William, in: The 11th International Symposium on Applications of Laser Techniques to Fluid Mechanics: Lisbon, Portugal: July 8-11, pp. 1–20. doi:10.1111/j.1349-7006.2001.tb02146.x.

Baral, B., Raine, R., Miskelly, G., 2011. Effect of engine operating conditions on spark-ignition engine pah emissions. SAE Technical Papers doi:10.4271/2011-01-1161.

Bardi, M., Pilla, G., Gautrot, X., 2019. Experimental assessment of the sources of regulated and unregulated nanoparticles in gasoline direct-injection engines. International Journal of Engine Research 20, 128–140. doi:10.1177/1468087418817448.

Bari, M.A., Baumbach, G., Kuch, B., Scheffknecht, G., 2010. Particle-phase concentrations of polycyclic aromatic hydrocarbons in ambient air of rural residential areas in southern Germany. Air Quality, Atmosphere & Health 3, 103–116. doi:10.1007/s11869-009-0057-8.

Bejaoui, S., Lemaire, R., Desgroux, P., Therssen, E., 2014. Experimental study of the e (m, λ)/e (m, 1064) ratio as a function of wavelength, fuel type, height above the burner and temperature. Applied Physics B 116, 313–323. doi:10.1007/s00340-013-5692-y.

Betrancourt, C., Liu, F., Desgroux, P., Mercier, X., Faccinetto, A., Salamanca, M., Ruwe, L., Kohse-Höinghaus, K., Emmrich, D., Beyer, A., et al., 2017. Investigation of the size of the incandescent incipient soot particles in premixed sooting and nucleation flames of n-butane using lii, him, and 1 nm-smps. Aerosol Science and Technology 51, 916–935. doi:10.1080/02786826.2017.1325440.

Betrancourt, C., Mercier, X., Desgroux, P., 2019. Quantitative measurement of volume fraction profiles of soot of different maturities in premixed flames by extinction-calibrated laser-induced incandescence. Applied Physics B: Lasers and Optics 125. doi:10.1007/s00340-018-7127-2.

Bhave, A., Kraft, M., 2004. Partially stirred reactor model: Analytical solutions and numerical convergence study of a pdf/monte carlo method. SIAM Journal of Scientific Computing 25, 93–104. doi:10.1137/S1064827502411328.

Bladh, H., Bengtsson, P.E., Delhay, J., Bouvier, Y., Therssen, E., Desgroux, P., 2006. Experimental and theoretical comparison of spatially resolved laser-induced incandescence (lii) signals of soot in backward and right-angle configuration. Applied Physics B 83, 423. doi:10.1007/s00340-006-2197-y.

Boiarciuc, A., Foucher, F., Mounam-Rousselle, C., Pajot, O., 2007. Estimate measurement of soot diameter and volume fraction inside the bowl of a direct-injection-compression-ignition engine: Effect of the exhaust gas recirculation. Combustion Science and Technology 179, 1631–1648. doi:10.1080/00102200701244728.

Cadle, S.H., Mulawa, P.a., Ball, J., Donase, C., Weibel, a., Sagebiel, J.C., Knapp, K.T., Snow, R., 1997. Particulate emission rates from in use high emitting vehicles recruited in Orange County, California. Environmental Science & Technology 31, 3405–3412. doi:10.1021/es9700257.

Carpentier, Y., Féraud, G., Dartois, E., Brunetto, R., Charon, E., Cao, A.T., D'Hendecourt, L., Bréchignac, P., Rouzaud, J.N., Pino, T., 2012. Nanostructuration of carbonaceous dust as seen through the positions of the 6.2 and 7.7 μm AIBs. Astronomy & Astrophysics 548, A40. doi:10.1051/0004-6361/201118700.

Case, M.K., Hofeldt, D.L., 1996. Soot mass concentration measurements in diesel engine exhaust using laser-induced incandescence. Aerosol Science and Technology 25, 46–60. doi:10.1080/02786829608965378.

Chasapidis, L., Melas, A.D., Tsakis, A., Zarvalis, D., Konstandopoulos, A., 2019. A Sampling and Conditioning Particle System for Solid Particle Measurements Down to 10 nm. Technical Report. SAE Technical Paper. doi:10.4271/2019-24-0154.

Cross, E.S., Sappok, A., Fortner, E.C., Hunter, J.F., Jayne, J.T., Brooks, W.A., Onasch, T.B., Wong, V.W., Trimborn, A., Worsnop, D.R., Kroll, J.H., 2012. Real-Time Measurements of Engine-Out Trace Elements: Application of a Novel Soot Particle Aerosol Mass Spectrometer for Emissions Characterization. Journal of Engineering for Gas Turbines and Power 134, 72801. doi:10.1115/1.4005992.

Dallmann, T.R., Onasch, T.B., Kirchstetter, T.W., Worton, D.R., Fortner, E.C., Herndon, S.C., Wood, E.C., Franklin, J.P., Worsnop, D.R., Goldstein, A.H., Harley, R.A., 2014. Characterization of particulate matter emissions from on-road gasoline and diesel vehicles using a soot particle aerosol mass spectrometer. Atmospheric Chemistry and Physics 14, 7585–7599. doi:10.5194/acp-14-7585-2014.

Delhay, J., Desgroux, P., Therssen, E., Bladh, H., Bengtsson, P.E., Hönen, H., Black, J.D., Vallet, I., 2009. Soot volume fraction measurements in aero-engine exhausts using extinction-calibrated backward laser-induced incandescence. Applied Physics B: Lasers and Optics 95, 825–838. doi:10.1007/s00340-009-3534-8.

Delhaye, D., Ouf, F.X., Ferry, D., Ortega, I.K., Penanhoat, O., Peillon, S., Salm, F., Vancassel, X., Focsa, C., Irimiea, C., Harivel, N., Perez, B., Quinton, E., Yon, J., Gaffie, D., 2017. The MERMOSE project: Characterization of particulate matter emissions of a commercial aircraft engine. Journal of Aerosol Science 105, 48–63. doi:10.1016/j.jaerosci.2016.11.018.

Donaldson, K., Li, X., MacNee, W., 1998. Ultrafine (nanometre) particle mediated lung injury. SIAM Journal of Scientific Computing 29, 553–560. doi:10.1016/S0021-8502(97)00464-3.

Duca, D., Irimiea, C., Faccinetto, A., Noble, J.A., Vojkovic, M., Carpentier, Y., Ortega, I.K., Pirim, C., Focsa, C., 2019. On the benefits of using multivariate analysis in mass spectrometric studies of combustion-generated aerosols. Faraday Discussions , 1–13doi:10.1039/C8FD00238J.

EPA, 2009. Integrated science assessment for particulate matter. Research Triangle Park, NC: US Environm Protection Agency EPA/600/R-08/139F. URL: https://cfpub.epa.gov/ncea/isa/recordisplay.cfm?deid=216546.

Etheridge, J., Mosbach, S., Kraft, M., Wu, H., Collings, N., 2011. Modeling soot formation in a disi engine. Proceedings of the Combustion Institute 33, 3159–3167. doi:10.1016/j.proci.2010.07.039.

European commision, 2017. Commission regulation (eu) 2017/1154. Official Journal of the European Union 1154, 708–732. doi:10.1016/j.proci.2010.07.039.

Faccinetto, A., Desgroux, P., Ziskind, M., Therssen, E., Focsa, C., 2011. High-sensitivity detection of polycyclic aromatic hydrocarbons adsorbed onto soot particles using laser desorption/laser ionization/time-of-flight mass spectrometry: An approach to studying the soot inception process in low-pressure flames. Combustion and Flame 158, 227–239. doi:10.1016/j.combustflame.2010.08.012.

Faccinetto, A., Focsa, C., Desgroux, P., Ziskind, M., 2015. Progress toward the Quantitative Analysis of PAHs Adsorbed on Soot by Laser Desorption/Laser Ionization/Time-of-Flight Mass Spectrometry. Environmental Science and Technology 49, 10510–10520. doi:10.1021/acs.est.5b02703.

Faccinetto, A., Thomson, K., Ziskind, M., Focsa, C., 2008. Coupling of desorption and photoionization processes in two-step laser mass spectrometry of polycyclic aromatic hydrocarbons. Applied Physics A: Materials Science and Processing 92, 969–974. doi:10.1007/s00339-008-4605-0.

de Francqueville, L., Bruneaux, G., Thirouard, B., 2010. Soot volume fraction measurements in a gasoline direct injection engine by combined laser induced incandescence and laser extinction method. SAE International Journal of Engines 3, 163–182. doi:10.2307/26275476.

Fushimi, A., Kondo, Y., Kobayashi, S., Fujitani, Y., Saitoh, K., Takami, A., Tanabe, K., 2016. Chemical composition and source of fine and nanoparticles from recent direct injection gasoline passenger cars: Effects of fuel and ambient temperature. Atmospheric Environment 124, 77–84. doi:10.1016/j.atmosenv.2015.11.017.

Gaddam, C.K., Wal, R.L.V., 2013. Physical and chemical characterization of SIDI engine particulates. Combustion and Flame 160, 2517–2528. doi:10.1016/j.combustflame.2013.05.025.

Giechaskiel, B., Manfredi, U., Martini, G., 2014. Engine exhaust solid sub-23 nm particles: I. literature survey. SAE International Journal of Fuels and Lubricants 7, 950–964. doi:10.4271/2014-01-2834.

Giechaskiel, B., Vanhanen, J., Vakeva, M., Martini, G., 2017. Investigation of vehicle exhaust sub-23 nm particle emissions. Aerosol Science and Technology 51, 626–641. doi:10.4271/2014-01-2834.

Gilardoni, S., Russell, L.M., Sorooshian, A., Flagan, R.C., Seinfeld, J.H., Bates, T.S., Quinn, P.K., Allan, J.D., Williams, B., Goldstein, A.H., Onasch, T.B., Worsnop, D.R., 2007. Regional variation of organic functional groups in aerosol particles on four U.S. east coast platforms during the International Consortium for Atmospheric Research on Transport and Transformation 2004 campaign. Journal of Geophysical Research Atmospheres 112, 1–11. doi:10.1029/2006JD007737.

Haefliger, O.P., Zenobi, R., 1998. Laser mass spectrometric analysis of polycyclic aromatic hydrocarbons with wide wavelength range laser multiphoton ionization spectroscopy. Analytical chemistry 70, 2660–2665. doi:10.1021/ac971264f.

Hansen, N., Klippenstein, S.J., Westmoreland, P.R., Kasper, T., Kohse-Höinghaus, K., Wang, J., Cool, T.A., 2008. A combined ab initio and photoionization mass spectrometric study of polyynes in fuel-rich flames. Physical chemistry chemical physics : PCCP 10, 366–374. doi:10.1039/b711578d.

Hong, S., Wooldridge, M., Im, H., Assanis, D., Pitsch, H., 2005. Development and application of a comprehensive soot model for 3D CFD reacting flow studies in a diesel engine. Combustion Flame 143, 11–26. doi:10.1016/j.combustflame.2005.04.007.

Huang, X., Olmez, I.O., Aras, N.K., Gordon, G.E., 1994. Emissions of trace elements from motor vehicules: Potential marker elements and source composition. Atmospheric Environment 28, 1385–1391. doi:10.1016/1352-2310(94)90201-1.

Irimiea, C., Faccinetto, A., Carpentier, Y., Ortega, I.K., Nuns, N., Therssen, E., Desgroux, P., Focsa, C., 2018. A comprehensive protocol for chemical analysis of flame combustion emissions by secondary ion mass spectrometry. Rapid Communications in Mass Spectrometry 32, 1015–1025. doi:10.1002/rcm.8133.

Irimiea, C., Faccinetto, A., Mercier, X., Ortega, I.K., Nuns, N., Therssen, E., Desgroux, P., Focsa, C., 2019. Unveiling trends in soot nucleation and growth: When secondary ion mass spectrometry meets statistical analysis. Carbon 144, 815–830. doi:10.1016/j.carbon.2018.12.015.

Karjalainen, P., Pirjola, L., Heikkila, J., Lahde, T., Tzamkiozis, T., Ntziachristos, L., Keskinen, J., Ronkko, T., 2014. Exhaust particles of modern gasoline vehicles : A laboratory and an on- road study. Atmospheric Environment 97, 262–270. doi:10.1016/j.atmosenv.2014.08.025.

Kayes, D., Hochgreb, S., Maricq, M.M., Podsiadlik, D.H., Chase, R.E., 2000. Particulate matter emission during start-up and transient operation of a spark-ignition engine (2): Effect of speed, load, and real-world driving cycles. SAE Technical Papers doi:10.4271/2000-01-1083.

Khalek, I.A., Bougher, T., Jetter, J.J., 2010. Particle emissions from a 2009 gasoline direct injection engine using different commercially available fuels. SAE International Journal of Fuels and Lubricants 3, 623–637. doi:10.4271/2010-01-2117.

Kirchner, U., Vogt, R., Natzeck, C., Goschnick, J., 2003. Single particle MS, SNMS, SIMS, XPS, and FTIR spectroscopic analysis of soot particles during the AIDA campaign. Journal of Aerosol Science 34, 1323–1346. doi:10.1016/S0021-8502(03)00362-8.

Kleeman, M.J., Riddle, S.G., Robert, M.A., Jakober, C.A., 2008. Lubricating oil and fuel contributions to particulate matter emissions from light-duty gasoline and heavy-duty diesel vehicles. Environmental Science and Technology 42, 235–242. doi:10.1021/es071054c.

Ko, J., Kim, K., Chung, W., Myung, C.L., Park, S., 2019. Characteristics of on-road particle number (PN) emissions from a GDI vehicle depending on a catalytic stripper (CS) and a metal-foam gasoline particulate filter (GPF). Fuel 238, 363–374. doi:10.1016/j.fuel.2018.10.091.

Koegl, M., Hofbeck, B., Will, S., Zigan, L., 2018. Investigation of soot formation and oxidation of ethanol and butanol fuel blends in a DISI engine at different exhaust gas recirculation rates. Applied Energy 209, 426–434. doi:10.1016/j.apenergy.2017.11.034.

Kong, S., Han, Z., Reitz, R., 1995. The development and application of a diesel ignition and combustion model for multidimensional engine simulations. SAE Technical Paper , 1–15doi:10.1016/j.combustflame.2005.04.007.

Kontses, A., Triantafyllopoulos, G., Ntziachristos, L., Samaras, Z., 2020. Particle number (pn) emissions from gasoline, diesel, lpg, cng and hybrid-electric light-duty vehicles under real-world driving conditions. Atmospheric Environment 222, 117–126. doi:10.1016/j.atmosenv.2019.117126.

Kristensson, A., Johansson, C., Westerholm, R., Swietlicki, E., Gidhagen, L., Wideqvist, U., Vesely, V., 2004. Real-world traffic emission factors of gases and particles measured in a road tunnel in Stockholm, Sweden. Atmospheric Environment 38, 657–673. doi:10.1016/j.atmosenv.2003.10.030.

Lai, J., Parry, O., Mosbach, S., Bhave, A., Page, V., 2018. Evaluating emissions in a modern compression ignition engine using multi-dimensional pdf-based stochastic simulations and statistical surrogate generation. SAE Technical Paper 2018-01-1739, 1–17. doi:10.4271/2018-01-1739.

Lee, K.F.K., Eaves, N., Mosbach, S., Ooi, D., Lai, J., Bhave, A., Manz, A., Geiler, J.N.J., Noble, J.A.J., Duca, D., Focsa, C., Niklas, J., Robert, G., Gmbh, B., Noble, J.A.J., Duca, D., 2019. Model Guided Application for Investigating Particle Number (PN) Emissions in GDI Spark Ignition Engines. SAE international 26, 1–13. doi:10.4271/2019-26-0062.Abstract.

Lemaire, R., Therssen, E., Desgroux, P., 2010. Effect of ethanol addition in gasoline and gasoline–surrogate on soot formation in turbulent spray flames. Fuel 89, 3952–3959. doi:10.1016/j.fuel.2010.06.031.

Li, Y., Zhang, L., Tian, Z., Yuan, T., Zhang, K., Yang, B., Qi, F., 2009. Investigation of the rich premixed laminar acetylene/oxygen/argon flame: Comprehensive flame structure and special concerns of polyynes. Proceedings of the Combustion Institute 32, 1293–1300. doi:10.1016/j.proci.2008.07.009.

Manke, A., Wang, L., Rojanasakul, Y., 2013. Mechanisms of nanoparticle-induced oxidative stress and toxicity. SAE Technical Paper 2013, 1–15. doi:10.1155/2013/942916.

Maricq, M.M., Szente, J., Loos, M., Vogt, R., 2011. Motor Vehicle PM Emissions Measurement at LEV III Levels. SAE International Journal of Engines 4, 597–609. doi:10.4271/2011-01-0623.

Marple, V.A., 2004. History of Impactors—The First 110 Years. Pakistan Textile Journal , 247–292doi:10.1080/02786820490424347.

Marple, V.A., Rubow, K.L., Behm, S.M., 1991. A microorifice uniform deposit impactor (moudi): Description, calibration, and use. Aerosol Science and Technology 14, 434–436. doi:10.1002/pssc.201600009.

McLafferty, F.W., Tureek, F., 1993. Interpretation of Mass Spectra. University Science Books, Mill Valley, CA.

Michelsen, H.A., Liu, F., Kock, B.F., Bladh, H., Boiarciuc, A., Charwath, M., Dreier, T., Hadef, R., Hofmann, M., Reimann, J., Will, S., Bengtsson, P.E., Bockhorn, H., Foucher, F., Geigle, K.P., Mounaim- Rousselle, C., Schulz, C., Stirn, R., Tribalet, B., Suntz, R., 2007. Modeling Laser-Induced Incandescence of Soot : A Summary and Comparison of LII Models. Applied Physics B: Lasers and Optics 87, 503–521. doi:10.1007/s00340-007-2619-5.

Mihesan, C., Ziskind, M., Therssen, E., Desgroux, P., Focsa, C., 2006. IR laser resonant desorption of polycyclic aromatic hydrocarbons. Chemical Physics Letters 423, 407–412. doi:10.1016/j.cplett.2006.04.032.

Mihesan, C., Ziskind, M., Therssen, E., Desgroux, P., Focsa, C., 2008. Parametric study of polycyclic aromatic hydrocarbon laser desorption. Journal of Physics: Condensed Matter 20, 25221. doi:10.1088/0953-8984/20/02/025221.

Moldanová, J., Fridell, E., Popovicheva, O., Demirdjian, B., Tishkova, V., Faccinetto, A., Focsa, C., 2009. Characterisation of particulate matter and gaseous emissions from a large ship diesel engine. Atmospheric Environment 43, 2632–2641. doi:10.1016/j.atmosenv.2009.02.008.

Momenimovahed, A., Handford, D., Checkel, M.D., Olfert, J.S., 2015. Particle number emission factors and volatile fraction of particles emitted from on-road gasoline direct injection passenger vehicles. Atmospheric Environment 102, 105–111. doi:10.1016/j.atmosenv.2014.11.045.

Oberdorster, G., 1996. Significance of particle parameters in the evaluation of exposure-dose relationships of inhaled particles. Inhalation Toxicology 8, 73–90. doi:10.1155/2013/942916.

Pagels, J., Dutcher, D.D., Stolzenburg, M.R., Mcmurry, P.H., Gälli, M.E., Gross, D.S., 2013. Fine-particle emissions from solid biofuel combustion studied with single-particle mass spectrometry: Identification of markers for organics, soot, and ash components. Journal of Geophysical Research Atmospheres 118, 859–870. doi:10.1029/2012JD018389.

Parent, P., Laffon, C., Marhaba, I., Ferry, D., Regier, T.Z., Ortega, I.K., Chazallon, B., Carpentier, Y., Focsa, C., 2016. Nanoscale characterization of aircraft soot: A high-resolution transmission electron microscopy, Raman spectroscopy, X-ray photoelectron and near-edge X-ray absorption spectroscopy study. Carbon 101, 86–100. doi:10.1016/j.carbon.2016.01.040.

Patil, N., Poul, A., Patil, A., Yerrawat, R.N., 2014. Literature Review on Effect of Oxygenated Additives on S.I. Engine Performance & Emissions. International Journal of Engineering, Business and Enterprise Applications 10, 73–76.

Pei, L., Jiang, G., Tyler, B.J., Baxter, L.L., Linford, M.R., 2008. Time-of-flight secondary ion mass spectrometry of a range of coal samples: A chemometrics (PCA, cluster, and PLS) analysis. Energy and Fuels 22, 1059–1072. doi:10.1021/ef7003199.

Pitz, W.J., Cernansky, N.P., Dryer, F.L., Egolfopoulos, F.N., Farrell, J.T., Friend, D.G., Pitsch, H., 2007. Development of an experimental database and chemical kinetic models for surrogate gasoline fuels. SAE Technical Papers , 1–13doi:10.4271/2007-01-0175.

Popovicheva, O.B., Irimiea, C., Carpentier, Y., Ortega, I.K., Kireeva, E.D., Shonija, N.K., Schwarz, J., Vojtíšek-Lom, M., Focsa, C., 2017. Chemical composition of diesel/biodiesel particulate exhaust by FTIR spectroscopy and mass spectrometry: Impact of fuel and driving cycle. Aerosol and Air Quality Research 17, 1717–1734. doi:10.4209/aaqr.2017.04.0127.

Price, P., Stone, R., Oudenijeweme, D., Chen, X., 2007. Cold start particulate emissions from a second generation di gasoline engine. SAE International 1931, 1738–1752. doi:10.4271/2007-01-1931.

Raza, M., Chen, L., Leach, F., Ding, S., 2018. A review of particulate number (pn) emissions from gasoline direct injection (gdi) engines and their control techniques. Energies 11, 1417–1443. doi:10.3390/en11061417.

Rencher, A., 2000. Methods of multivariate analysis. Journal of Statistical Planning and Inference 59, 183–194. doi:10.1016/

S0378-3758(96)00098-5.
Sadezky, A., Muckenhuber, H., Grothe, H., Niessner, R., Pöschl, U., 2005. Raman microspectroscopy of soot and related carbonaceous materials: Spectral analysis and structural information. Carbon 43, 1731–1742. doi:10.1016/j.carbon.2005.02.018.
Sager, T., Castranova, V., 2009. Surface area of particle administered versus mass in determining the pulmonary toxicity of ultrafine and fine carbon black: Comparison to ultrafine titanium dioxide. Journal of Statistical Planning and Inference 6, 1–15. doi:10.1186/1743-8977-6-15.
Sakurai, H., Tobias, H.J., Park, K., Zarling, D., Docherty, K.S., Kittelson, D.B., McMurry, P.H., Ziemann, P.J., 2003. On-line measurements of diesel nanoparticle composition and volatility. Atmospheric Environment 37, 1199–1210. doi:10.1016/S1352-2310(02)01017-8.
Schulz, C., Kock, B.F., Hofmann, M., Michelsen, H., Will, S., Bougie, B., Suntz, R., Smallwood, G., 2006. Laser-induced incandescence: Recent trends and current questions. Applied Physics B: Lasers and Optics 83, 333–354. doi:10.1007/s00340-006-2260-8.
Seaton, A., Tran, L., Aitken, R., Donaldson, K., 2009. Surface area of particle administered versus mass in determining the pulmonary toxicity of ultrafine and fine carbon black: Comparison to ultrafine titanium dioxide. Journal of the Royal Society Interface 7, S119–S129. doi:10.1186/1743-8977-6-15.
Simonen, P., Kalliokoski, J., Karjalainen, P., Rönkkö, T., Timonen, H., Saarikoski, S., Aurela, M., Bloss, M., Triantafyllopoulos, G., Kontses, A., et al., 2019. Characterization of laboratory and real driving emissions of individual euro 6 light-duty vehicles–fresh particles and secondary aerosol formation. Environmental Pollution 255, 113175. doi:10.1016/j.envpol.2019.113175.
Smallbone, A., Bhave, A., Coble, A., Mosbach, S., Kraft, M., Morgan, N., Kalghatgi, G., 2011. Simulating pm emissions and combustion stability in gasoline/diesel fuelled engines. Journal of the Royal Society Interface 2011-01-1184, 1–17. doi:10.4271/2011-01-1184.
Smallwood, G.J., Snelling, D.R., Ömer L. Gülder, Clavel, D., Gareau, D., Sawchuk, R.A., Graham, L., 2001. Transient particulate matter measurements from the exhaust of a direct injection spark ignition automobile. SAE Transactions 110, 1948–1962. doi:10.2307/44742794.
Swanson, J., Kittelson, D., Twigg, M., 2013. A Miniature Catalytic Stripper for Particles Less Than 23 Nanometers. SAE International 1570, 542–551. doi:10.4271/2013-01-1570.
Thomson, K., Ziskind, M., Mihesan, C., Therssen, E., Desgroux, P., Focsa, C., 2007. Influence of the photoionization process on the fragmentation of laser desorbed polycyclic aromatic hydrocarbons. Applied Surface Science 253, 6435–6441. doi:10.1016/j.apsusc.2007.01.050.
Tobias, H.J., Beving, D.E., Ziemann, P.J., Sakurai, H., Zuk, M., McMurry, P.H., Zarling, D., Waytulonis, R., Kittelson, D.B., 2001. Chemical analysis of diesel engine nanoparticles using a nano-DMA/thermal desorption particle beam mass spectrometer. Environmental Science & Technology 35, 2233–2243. doi:10.1021/es0016654.
Velji, A., Yeom, K., Wagner, U., Spicher, U., Roßbach, M., Suntz, R., Bockhorn, H., 2009. Investigations of the formation and oxidation of soot inside a direct injection spark ignition engine using advanced laser-techniques. SAE Paper 2010-01-0352, 1–14. doi:10.4271/2010-01-0352.
Vojtíšek, M., Beránek, V., Matušů, R., Štolcpartová, J., 2014. Particle emmissions from gasoline automobiles – a preliminary comparison between direct and port fuel injection and across driving cycles, in: XLV International Scientific Conference of the Czech and Slovak University Departments and Institutions Dealing with the Research of Internal Combustion Engines, pp. 2–8.
Vojtisek-Lom, M., Fenkl, M., Dufek, M., Mareš, J., 2009. Off-cycle, real-world emissions of modern light duty diesel vehicles. SAE Technical Papers 2009-24-01, 1–22. doi:10.4271/2009-24-0148.
Wang, C., Xu, H., Herreros, J.M., Lattimore, T., Shuai, S., 2014. Fuel effect on particulate matter composition and soot oxidation in a direct-injection spark ignition (disi) engine. Energy & Fuels 28, 2003–2012. doi:10.1021/ef402234z.
Wang, G., Kawamura, K., Xie, M., Hu, S., Gao, S., Cao, J., An, Z., Wang, Z., 2009. Size-distributions of n-alkanes, PAHs and hopanes and their sources in the urban, mountain and marine atmospheres over East Asia. Atmospheric Chemistry and Physics 9, 8869–8882. doi:10.5194/acp-9-8869-2009.
Weiss, M., Bonnel, P., Hummel, R., Provenza, A., Manfredi, U., 2011. On-road emissions of light-duty vehicles in Europe. Environmental Science and Technology 45, 8575–8581. doi:10.1021/es2008424.
Williams, M., Minjares, R., 2016. A technical summary of Euro 6/VI vehicle emission standards. ICCT (International Council on Clean Transportation) Briefing , 1–17. URL: https://theicct.org/publications/technical-summary-euro-6vi-vehicle-emission-standards.
Williams, T.C., Shaddix, C.R., Schefer, R.W., Desgroux, P., 2007. The response of buoyant laminar diffusion flames to low-frequency forcing. Combustion and flame 151, 676–684. doi:10.1016/j.combustflame.2007.07.023.
World Health Organization, 2013. Health effects of particulate matter. policy implications for countries in eastern europe. caucasus and central asia. World Health Organization Regional Office for Europe. URL: http://www.euro.who.int/__data/assets/pdf_file/0006/189051/Health-effects-of-particulate-matter-final-Eng.pdf.
Wu, S., Yang, W., Xu, H., Jiang, Y., 2019a. Investigation of soot aggregate formation and oxidation in compression ignition engines with a pseudo bi-variate soot model. Applied Energy 253, 113609. doi:10.1016/j.apenergy.2019.113609.
Wu, S., Zhou, D., Yang, W., 2019b. Implementation of an efficient method of moments for treatment of soot formation and oxidation processes in three-dimensional engine simulations. Applied Energy 254, 113661. doi:10.1016/j.apenergy.2019.113661.
Zheng, Z., Johnson, K.C., Durbin, T.D., Hu, S., Huai, T., Kittelson, D.B., Jung, H.S., 2011. Investigation of solid particle number measurement: Existence and nature of sub 23 nm particles under PMP methodology. Fall Technical Meeting of the Western States Section of the Combustion Institute 2011, WSS/CI 2011 Fall Meeting 42, 455–461. doi:10.1016/j.jaerosci.

2011.08.003.
Zimmermann, R., Blumenstock, M., Heger, H.J., Schramm, K.W., Kettrup, A., 2001. Emission of nonchlorinated and chlorinated aromatics in the flue gas of incineration plants during and after transient disturbances of combustion conditions: Delayed emission effects. Environmental Science and Technology 35, 1019–1030. doi:10.1021/es0001431.